Director anchoring on a simple edge dislocation at the surface of induced smectic-C_A films

Yves Galerne ⬤

Université de Strasbourg, CNRS, Institut de Physique et Chimie des Matériaux de Strasbourg, UMR 7504, F- 67000 Strasbourg, France

We present a detailed analysis of *c*-director anchoring measurements on simple edge dislocations at the surface of smectic-C_A films (steps). Indications show that the *c*-director anchoring on the dislocations originates from a local and partial melting of the dislocation core that depends on the anchoring angle. The SmC_A films are induced on isotropic puddles of 1-(methyl)-heptyl-terephthalylidene-bis-amino cinnamate molecules by the surface field, while the dislocations are located at the isotropic-smectic interface. The experimental setup is based on the connection of a three-dimensional smectic film sandwiched between a one-dimensional edge dislocation on its lower surface, and a two-dimensional surface polarization spread over the upper surface. Applying an electric field produces a torque that balances the anchoring torque of the dislocation. The film distortion that results is measured under a polarizing microscope. Exact calculations on these data, anchoring torque versus director angle, yield the anchoring properties of the dislocation. A specificity of our sandwich configuration is to improve the measurement quality by a factor of $N^{3/2} \sim 600$, where $N = 72$ is the number of smectic layers in the film. We fit a second-order Fourier series on the torque-anchoring angle data, which has the advantage of *converging uniformly* over the entire anchoring angle range, i.e., over more than $70°$. The two corresponding Fourier coefficients, k_{a1}^{F2} and k_{a2}^{F2}, are anchoring parameters that generalize the usual anchoring coefficient. When changing the electric field $\boldsymbol{E}$, the anchoring state evolves along paths in a torque-anchoring angle diagram. Two cases occur depending on the angle α_∞ of $\boldsymbol{E}$ relative to the unit vector $\boldsymbol{S}$, perpendicular to the dislocation and parallel to the film. When $\alpha_\infty < 130°$, the operating point $\boldsymbol{Q}$ that represents the anchoring state in the diagram follows reversible and "at-equilibrium" paths. Its free displacement velocity is infinitely slow, so that we have to push it with electric torque steps smaller than the experimental error bar $\delta\Gamma \sim 10^{-14}$N. On the other hand, for $\alpha_\infty > 130°$, $\boldsymbol{Q}$ describes a hysteresis loop similar to the usually encountered ones in solids. This loop connects two states that exhibit broken and nonbroken anchorings, respectively. The paths that join them in an out-of-equilibrium process are irreversible and dissipative. When coming back to a nonbroken anchoring state, both the dislocation and smectic film spontaneously heal back in the very same state they were before the anchoring broke. The process does not produce any *erosion* thanks to their liquid nature, including at the microscopic scale. The energy that is dissipated on these paths is roughly estimated in terms of the *c*-director rotational viscosity. Similarly, we can evaluate the maximum time of flight along the dissipative paths to be of the order of a few seconds, which is consistent with qualitative observations. In contrast, the paths located inside each domain of these anchoring states are reversible and can be followed in an "at equilibrium" manner all along. This analysis should provide a basis for understanding the structure of multiple edge dislocations in terms of parallel simple edge dislocations interacting with each other through pseudo-Casimir forces arising from *c*-director thermodynamic fluctuations between them.

I. INTRODUCTION

Among the interesting things that can be observed in liquid crystals with a simple polarizing microscope are the smectic films that spontaneously grow at the free surface of isotropic droplets or puddles of pure mesogenic compounds. They are induced by the molecular field on the free surface, at a temperature above the bulk isotropic to smectic phase transition. With 1-(methyl)-heptyl-terephthalylidene-bis-amino cinnamate (MHTAC), a nonchiral compound, the film forms in an unlimited layer-by-layer process with slowly decreasing temperature. Each new layer in the film is initiated by an edge dislocation of Burgers vector equal to unity at the isotropic-smectic phase interface. Being located at the interface with a nematic layer, the edge dislocation is a surface edge dislocation and may be called a step for short. The

epitaxial process then goes on repetitively and perfectly deposits parallel smectic layers one after the other [1].

Combined interferential measurements, at normal and oblique incidences, show that a first mesophasic layer forms uniformly over the whole surface of isotropic puddles, several degrees above the isotropic-smectic phase transition, $T_{\mathrm{Sm}} = 158\,°$C [2], and it gradually lightens on decreasing temperature when observed between crossed polarizers. These continuous properties, not preceded by any dislocation, indicate that a first nematic layer is created. Its thickness may be identified to the correlation length of the orientational order, i.e., to the correlation length of the nematic order in the isotropic phase. This layer thickness increases while reducing the temperature, until reaching the value $\xi \sim 7$ nm when the first smectic layer begins to form [1]. On slowly decreasing temperature again, smectic layers then form one by one at the

nematic interface in contact with the air (for the first smectic layer) or in contact with the smectic layers already formed. They start with an edge dislocation, each one corresponding to a different front of the first-order transition from the nematic to smectic phase. The thickness of the smectic layers being measured to be $l_{Sm} = 3$ nm, the number of simple dislocations that pass across the observation field allows one to count the exact number of smectic layers at this point of the film, and consequently to determine its thickness. With faster cooling temperature, multiple edge dislocations may form. Under a polarized light microscope, they appear to be thicker than simple ones and cannot be confused with them.

An electric field E applied parallel to the film by means of electrodes evaporated on the glass substrate produces walls in the film [1]. The compound being nonchiral, the plane of the molecules (x, z) is a symmetry plane of the film that contains both the **c**-director and the electric polarization of the film P. The y-axis is taken along the edge dislocation (Fig. 1). The elastic and electric energies involved in the film are proportional to $\frac{K}{w^2}$ and PE, respectively, w being the width of the observed walls, and K the average elastic constant of the film. At equilibrium, these energies being equal, the squared wall width w^2 is on the order of magnitude of $\frac{K}{PE}$; cf. Sec. II A. Moreover, the w measurements show to within 5% accuracy that w^2 is proportional to the film thickness. With the elastic constant of the film, K, being also proportional to the film thickness, because the elasticity of each smectic layer adds up to the other ones, both the film thickness variations in w^2 and in K compensate for each other. We deduce that the tangential polarization on the film surface, P, is independent of film thickness. P is thus a surface polarization, and more exactly, P is the addition of two surface polarizations, one on each side of the smectic film. Therefore, according to the parity of N, which is the number of smectic layers in the film, P is the sum or the difference between the two polarizations on the film surfaces in contact with the air and in contact with the isotropic phase, respectively. With the measured film polarization being independent of the parity of N, within the error bars, one of these surface polarizations is negligible compared to the other one. We deduce that P is mainly spread over one of these two surfaces. As moreover the direction of the polarization is the same on both sides of the dislocation, for $x > 0$ and for $x < 0$, we understand that the polarization is indeed located on the opposite surface from the edge dislocations, i.e., on the smectic layer in contact with the air. This P direction consequently identifies with the direction of the film director, c, which is therefore also attached to the free surface in contact with the air [Fig. 1(a)].

As already noticed [2], the dislocation lines appear thicker under a polarizing microscope when E is applied from an odd N region of the film to a region with an even N than when E is oriented in the opposite direction. In the former case, E produces a larger distortion than when applied along the preferred anchoring direction of c on the dislocation. This gives a thicker appearance to the dislocation. This detail also shows that though located on the upper air-smectic interface, the **c**-director anchors on the dislocation that is indeed situated on the internal smectic-isotropic interface, on the other side of the film. More precisely, **c** anchors along the unit vector S, parallel to the film, perpendicular to the dislocation line, and
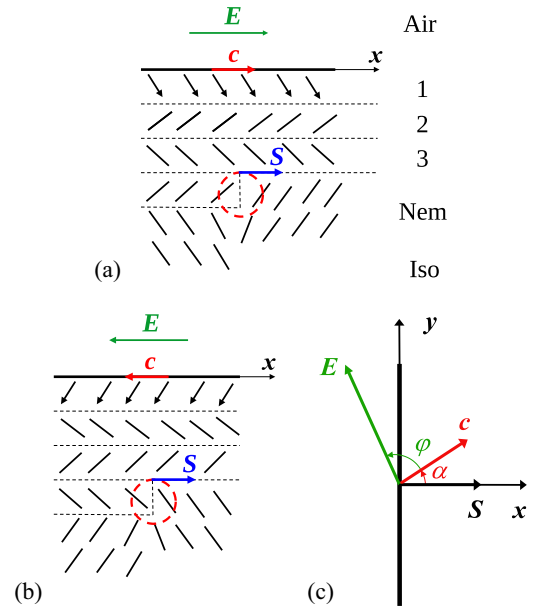

FIG. 1. (a) Cross-section of a SmC$_A$ film at the free surface of a nonchiral MHTAC puddle, showing three smectic layers ahead of a surface edge dislocation (step) and four smectic layers behind it. A Burgers circuit running horizontally in the air and in the nematic phase, and vertically closed on both sides through the broken lines that delimit the smectic layers, could be drawn in panels (a) or (b). Crossing four layers on one side and three on the other side, such a circuit would show that the Burgers vector of the dislocation is equal to one layer thickness. The dislocation is along the y-axis, perpendicular to panel (a). Its core is marked by a red dashed circle. The tilt of the molecules is reduced in the first SmC$_A$ layer (arrows depict their individual electric polarization) and in the nematic layer in contact with and above the isotropic phase (the molecules are not shown). The projection of the molecules onto the film defines the **c**-director, which is parallel to the horizontal component of the surface polarization, P. For simplification, the electric field, E, is also oriented along the x-axis in this figure. (b) Dislocation core when reversing E and consequently P and c, from their orientations in (a). Note the sharper shape of the smectic molecules organization at the edge of the dislocation when compared to (a). (c) Top view of the film showing the applied electric field E, in a nonspecific orientation, the **c**-director at a distance x from dislocation, and the unit vector S, parallel to the smectic film, perpendicular to the edge dislocation, and oriented from the region containing an even number of smectic layers to an odd one. The angles of E and c relative to S are equal to α_∞ and α, respectively. In the experiment discussed here, $\alpha_\infty = 116°$.

oriented from the even-N region to the odd-N one. This means that both the orientational and positional organization of the molecules in the vicinity of dislocation cores are determined in a *unique* manner by means of *short-range* interactions $\sim l_{Sm}$. The molecular organization around dislocation cores thus resists deviations, and it is able to maintain the **c**-director close to its preferred anchoring direction, that is, along S as well as possible. So, the local molecular organization imposes that **c** and S reverse sign relative to each other each time a new smectic layer is added to the film according to a step-by-step mechanism. This *epitaxial process* thus builds up the exact tilt alternation of the molecules by means of interactions between molecules in direct contact from a smectic layer to the next

one. It is therefore useless to invoke any exotic long-range interaction mechanism to explain the perfectly alternate tilt structure that is observed in the SmC_A phase, all the more since such an argument should not be valid to explain that the first smectic layer alternates relative to the nematic layer, too. Surprisingly, taking advantage of the MHTAC ability to grow induced films almost indefinitely, the mechanism can be observed to extend from $N = 2$ to more than $N = 700$ without implying any detectable error. This experiment indeed demonstrates the stability and robustness of the alternate structure [2].

Interestingly, the same conclusions regarding the exact alternation of the tilt between smectic layers and the surface polarization can be extended to induced films of chiral MHTAC*. In addition, each smectic layer of the film exhibits a chiral or ferroelectric polarization P^* as in the SmC^* phases. This chiral polarization points in a direction perpendicular to the molecules and parallel to the smectic layers. Its direction is therefore reversed between neighboring layers since their tilts are alternately positive and negative. The overall structure of the chiral smectic phase is thus antiferroelectric [3]. Naturally, a helical distortion of the structure superimposes also on the results obtained with the racemate MHTAC. The measurements of the total polarization of the film, modulus and direction, as a function of the smectic layer number in the films, N, are consistent again with an exact alternation of the tilt, a rotation by $3°$ per layer, and separate volume and surface polarizations. The good agreement between the measurements and their calculations based on the hypothesis of a precise tilt alternation clearly corroborates the structure accurately, and thus provides a good confirmation that the SmO phase exactly exhibits an alternate tilt from a smectic layer to the next one, with a bulk period of $2l_{Sm}$.

Before these measurements, a SmC_A phase—for a tilted smectic phase with antiferroelectric properties—was published to be biaxial on the basis of conoscopic measurements in 4-(1-methylheptyloxycarbonyl)-phenyl-4′-octyloxybiphenyl-4-carboxylate (MHPOBC) [4]. These measurements meant that the tilt of the molecules in the layers was alternate, possibly *in the average*, or if periodic, different periods than $2l_{Sm}$, the SmO period, could not be excluded directly. To verify this point, mixing tests between SmO and SmC_A were performed. Heppke *et al.* indeed observed that a continuous path exists between the two phases on gradually mixing both MHTAC and MHPOBC compounds together. In this manner, they obtained real proof that both phases SmO and SmC_A were identical [5], and that it was no longer necessary to name them differently.

II. ANCHORING ON EDGE DISLOCATIONS

Simple edge dislocations in the SmC_A phase of MHTAC have interesting physical properties. They are essentially liquid and free from contacts with solids, or several millimeters apart, when observed in induced films. Interestingly, the elastic properties of the film can be used to weigh the extremely small torques that the dislocation exerts on the *c*-director. In the experiments that are analyzed here, an electric field E is addressed parallel to a SmC_A film by means of electrodes evaporated 2 mm apart on a glass substrate on which a small

amount of MHTAC is deposited. The applied electric field E couples with the surface polarization P and produces a torque that at equilibrium matches the anchoring torque. From the amplitude and direction of E, we calculate the applied torque, but before using these smectic films as microbalances for measuring the anchoring torques exerted by edge dislocations, we need to revisit their calibration. Such an improvement could provide an opportunity to estimate the interaction between edge dislocations at small distances. Before addressing such questions where pseudo-Casimir interactions should be involved until binding simple edge dislocations into multiple ones, we need to come back to the anchoring strength measurements of the *c*-director on surface edge dislocations which previously were insufficiently well analyzed [6].

A. 2D elastic distortion

In each smectic layer, the molecules are oriented along a unit vector **n**, equivalent to the nematic director. To express its coordinates, we use a reference frame where the **z**-axis is perpendicular to the film, and the **x**-axis is along the unit vector S, parallel to the smectic layer, perpendicular to the edge dislocation (or step), and oriented from the even-N region to the odd-N one. The **n** coordinates, for the considered smectic layer, are thus given by $\begin{vmatrix} \sin\Psi\cos\alpha \\ \sin\Psi\sin\alpha \\ \cos\Psi \end{vmatrix}$, where Ψ and α are the average tilt and azimuthal angles of the molecules, respectively. As the film is not chiral, nor submitted to any stress around the **z** axis, we see that the film does not undergo any twist. Its elastic energy density, i.e., per volume unit, is then reduced to

$$f_\mathcal{K} = \tfrac{1}{2}\mathcal{K}_{11}(\nabla \cdot \mathbf{n})^2 + \tfrac{1}{2}\mathcal{K}_{33}(\mathbf{n} \wedge (\nabla \wedge \mathbf{n}))^2, \qquad (1)$$

where K_{11} and K_{33} are the Frank elastic constants for splay and bend distortions, respectively. Assuming an average value of $K \sim 5 \times 10^{-12}$ N, the measurements of the wall widths, w, lead to the determination of the projected polarization on the film, $P = 3.1 \times 10^{-14}$ C/m [1], and to the evaluation of an anisotropy of elasticity, $\frac{\mathcal{K}_{11}-\mathcal{K}_{33}}{2\mathcal{K}} \sim 2.3$. This corresponds to a ratio $\frac{\mathcal{K}_{33}}{\mathcal{K}_{11}} \sim 0.43$, which seems small when compared to elastic ratios obtained from nematic liquid crystals, since data are lacking for tilted smectics. Thus, $\frac{\mathcal{K}_{33}}{\mathcal{K}_{11}}$ is found to span from 1.3 to 1.4 depending on temperature, in 4-4′-n-pentyl-cyanobiphenyl (5CB), or from 1.7 to 2.03 in 4- (trans-4′-n pentylcyclohexyl) -benzonitrile (PCH-5) [7]. Numerous measurements confirm that such a ratio $\frac{\mathcal{K}_{33}}{\mathcal{K}_{11}}$ is larger than 1 in normal nematic liquid crystals [8]. However, based on molecular theory and computer simulations, Osipov *et al.* proposed that such small ratios $\frac{\mathcal{K}_{33}}{\mathcal{K}_{11}}$ were consistent with a large short-range smecticlike ordering. Such a property is clearly the case in the MHTAC SmC_A phase [9]. More recently, small ratios $\frac{\mathcal{K}_{33}}{\mathcal{K}_{11}}$ were also found in discotic nematic liquid crystal [10]. All these results, therefore, confirm that in our case, the ratio $\frac{\mathcal{K}_{33}}{\mathcal{K}_{11}}$ is anomalously small, and that it is indeed not possible to approximate it to unity as is currently done, e.g., in Refs. [6] and [11].

The elastic energy density f_K can be written in terms of the smectic *c*-director, which is defined in a tilted smectic as the projection of **n** onto the smectic plane, i.e., $\mathbf{c} = \sin\Psi \times \begin{vmatrix} \cos\alpha \\ \sin\alpha \end{vmatrix}$.

The elastic energy of a two-dimensional (2D) distortion per film surface unit can thus be written as

$$f_K = \tfrac{1}{2} K_s (\nabla \cdot \mathbf{c})^2 + \tfrac{1}{2} K_b (\mathbf{c} \wedge (\nabla \wedge \mathbf{c}))^2, \tag{2}$$

where $\{ {K_s = N\, l_{Sm}\, \mathcal{K}_{11} \sin^2 \Psi \atop K_b = N\, l_{Sm}\, \mathcal{K}_{33} \sin^4 \Psi}$ are the 2D splay and bend elastic constants of the film, $N\, l_{Sm}$ being the film thickness [11]. In the cases of nonstressed SmC_A films of MHTAC, Ψ is roughly a constant, $\Psi \sim 50°$. Moreover, we only consider a unidirectional distortion in the film, along the $\mathbf{y}$-axis and defined by the azimuthal angle $\alpha(x)$. With these restrictions, the 2D elastic energy can simply be written as $f_K = \tfrac{1}{2}[K - \delta K \cos 2\alpha](\frac{\partial \alpha}{\partial x})^2$, where we have introduced the average and difference between the two elastic constants of the film $\{ {K = \frac{1}{2}(K_s + K_b) \atop \delta K = \frac{1}{2}(K_s - K_b)}$. With the above figures, we have $K = N \times 7.5 \times 10^{-21}$ J. We thus deduce $w = \sqrt{N/E} \times 0.5$ mm. In the following, we use the relative elastic anisotropy $\chi = \frac{\delta K}{K}$, so that

$$f_K = \frac{1}{2} K[1 - \chi \cos 2\alpha]\left(\frac{\partial \alpha}{\partial x}\right)^2. \tag{3}$$

When an electric field $\mathbf{E}$ is applied parallel to the smectic film, the film contains an electric energy per surface unit:

$$f_E = -PE \cos(\alpha_\infty - \alpha). \tag{4}$$

In this expression, $\mathbf{P}$ is the horizontal component of the surface polarization carried by the first smectic layer in contact to the air. α and α_∞ are the angles of $\mathbf{P}$ and $\mathbf{E}$ relative to the $\mathbf{y}$-axis, respectively. Incidentally, this smectic layer and the nematic one at the smectic-isotropic interface of the film are less tilted than in the bulk ones [2].

Minimizing the free energy of the whole film yields the Euler-Lagrange equation:

$$[1 - \chi \cos 2\alpha]\frac{\partial^2 \alpha}{\partial x^2} + \chi \sin 2\alpha \left(\frac{\partial \alpha}{\partial x}\right)^2 - w^{-2} \sin(\alpha - \alpha_\infty)$$
$$= 0, \tag{5}$$

where $w = \sqrt{\frac{K}{PE}}$ is the characteristic distance of a distortion produced by an electric field, often called the wall width. To within a factor K, Eq. (5) is the equation of the torques that the $\mathbf{c}$-director undergoes in a SmC_A film, due to a unidirectional distortion along the $\mathbf{y}$-axis. The two first terms and the last one stand for the elastic and the electric torques, respectively. Indeed, these calculations generalize both the results obtained in Refs. [6] and [11], and which were restricted to cases in which analytic calculations were possible. In Ref. [6], the elastic constants were considered to be equal, but with $\chi = 0.6$ for MHTAC as found in Ref. [11], such an approximation is no longer acceptable. In Ref. [11], however, the calculation was limited to particular cases in which the electric field $\mathbf{E}$ is applied parallel or perpendicular to the $\mathbf{x}$-axis, i.e., such that $\alpha_\infty = 0$ or $\alpha_\infty = \infty$, where again analytic calculations could be performed.

Here, we directly consider the general case in which both χ and α_∞ take general values. We may expect that the detailed knowledge of the anchoring properties on dislocations will impact the director fluctuations in the interval between them, and could therefore affect the pseudo-Casimir energy in this region [12]. In this manner, the anchoring properties on the dislocations could be a key for calculating the interactions between dislocations, and they could consequently help to elucidate the formation of higher Burgers vector dislocations. Numerical calculations will be necessary to finish such calculations. Before this last step, analytic calculations remain possible. We can thus integrate Eq. (5) to

$$[1 - \chi \cos 2\alpha]\left(\frac{\partial \alpha}{\partial x}\right)^2 - 2w^{-2}[1 - \cos(\alpha - \alpha_\infty)] = A, \tag{6}$$

where A is an integration constant that can be shown to be zero by observing that when $x \to \infty$, $\frac{\partial \alpha}{\partial x} \to 0$ and $\alpha \to \alpha_\infty$. We deduce the equation of the distortion

$$\frac{\partial \alpha}{\partial x} = \frac{2}{w} \frac{\sin \frac{(\alpha_\infty - \alpha)}{2}}{\sqrt{1 - \chi \cos 2\alpha}}. \tag{7}$$

The derivative $\frac{\partial \alpha}{\partial x}$ originates from a square root. Its sign is *a priori* undetermined. However, the two angles α and α_∞, when considered in the 2π space $L_2[-\pi, \pi]$, have the same sign before α reaches its limit value α_∞. We deduce that the difference α_∞-α and the derivative $\frac{\partial \alpha}{\partial x}$ have the same sign. This property confirms that the sign chosen in Eq. (7) is correct.

B. Anchoring energy on a simple edge dislocation

The sketch in Fig. 1(c) shows the vectors $\mathbf{E}$, $\mathbf{c}$ (along $\mathbf{P}$), and $\mathbf{S}$, namely the electric field, the director, and the unit vector normal to the dislocation, respectively. The measurements are performed with the angle $[\mathbf{S}, \mathbf{E}] = \alpha_\infty = 116°$, and contrary to Ref. [6], we now take into account the evidence that in the SmC_A films of MHTAC, the 2D elastic constants K_s and K_b are much different from each other with a ratio $\frac{K_s}{K_b} \sim 4$. We are thus far from the one-elastic-constant hypothesis that we have used earlier for simplification [11]. We present now more detailed calculations.

The torque Γ_E and the anchoring torque Γ_a that the electric field $\mathbf{E}$ and the dislocation, respectively, exert on the smectic film produce an elastic distortion. At equilibrium, they balance each other, so that

$$\Gamma_E + \Gamma_a = 0. \tag{8}$$

With this equation, we deduce the anchoring torque Γ_a that the dislocation exerts on the film as a function of the electric field $\mathbf{E}$ and of the measured anchoring angle α_0 on the dislocation, i.e., at $x = 0$. Integrating over the whole film surface, or equivalently, integrating from the dislocation at $x = 0$, until $+\infty$ and multiplying by 2, we have

$$\Gamma_E = 2PE \int_0^\infty \sin(\alpha_\infty - \alpha)dx. \tag{9}$$

Using Eq. (7), which describes the distortion, the electric torque that is transmitted by the smectic film to each dislocation length unit becomes

$$\Gamma_E = 2\sqrt{PEK} \int_{\alpha_0}^{\alpha_\infty} \cos\left(\frac{\alpha_\infty - \alpha}{2}\right) \sqrt{1 - \chi \cos 2\alpha}\, d\alpha. \tag{10}$$

This integral replaces the approximate expression previously used to calculate the electric torque applied to the film [Eq. (4) in Ref. [6]]. However, a numerical integration is necessary to complete the electric torque calculation, Γ_E, as a function of the electric field $\boldsymbol{E}$, i.e., as a function of its amplitude E, and the angle from the $\boldsymbol{x}$-axis, α_∞; cf. Fig. 1(c).

As discussed above, the $\boldsymbol{c}$-director orients preferentially along $\boldsymbol{S}$, the anchoring direction generally called the easy axis, cf. Fig. 1(c). The anchoring energy then exhibits a minimum on the dislocation at $\alpha_0 = 0$. Such a property is due to the plane $(\boldsymbol{x},\boldsymbol{z})$ that, being perpendicular to the dislocation, is also a symmetry plane for the film structure (Fig. 1). Consequently, the anchoring energy is the same for $+\alpha_0$ and $-\alpha_0$, which means that the anchoring energy of the $\boldsymbol{c}$-director on the dislocation is an even function of α_0. The anchoring energy can thus be expressed in terms of $\cos\alpha_0$. Such an experimental observation of a director that orients perpendicularly to some limiting object somehow extends the well-known homeotropic anchoring, experienced by nematic liquid crystals on 2D surfaces. However, in this case, the director $\boldsymbol{n}$ is equivalent to $-\boldsymbol{n}$, so that the anchoring angle α_0 is also equivalent to $\alpha_0 + \pi$. This means that the anchoring energy is indeed a function of $\cos^2\alpha_0$, or equivalently, a function of $\sin^2\alpha_0$ to within some constant, a remark that was formulated a long time ago by Rapini-Papoular [13]. To obtain a better simulation of the anchoring energy as a function of α_0, Yang *et al.* proposed to use higher-order expansions in power series of $\sin^{2n}\alpha_0$ [14]. In fact, such an expansion may not be a real improvement to describe the anchoring properties in the case of weak anchorings, because the director should then experience large α_0 deviations from the equilibrium angle where the expansion is performed. In such a case, the anchoring angle could cover a larger domain than the convergence radius of the series, meaning that the expansion is indeed unable to fit on the whole experimental data range. Moreover, the successive terms of the series $\sin^{2n}\alpha_0$ are not orthogonal relative to one another, which causes the coefficients of the series to be somewhat unstable when climbing to higher expansion orders. For this reason, Barbero *et al.* suggested to use Fourier expansions [15], but without practical use as far as we know.

However, the $\boldsymbol{c}$-director of SmC_A films is a true vector, so that $\boldsymbol{c}$ is not equivalent to its opposite $-\boldsymbol{c}$. Its anchoring properties therefore do not exhibit the symmetry $\alpha_0 \leftrightarrow \alpha_0 + \pi$, and, in particular, the anchoring energy can directly be expressed in terms of $\cos\alpha_0$. Consequently, the Rapini-Papoular rule is not valid any more for edge dislocations in SmC_A films. This is a second reason to prefer Fourier expansions.

Moreover, Fourier expansions have a more decisive advantage, since they *converge uniformly* towards the original function over the entire available range, that is, $[0, \pi]$ and indeed $[0, 2\pi]$, when applying the $\alpha_0 \leftrightarrow -\alpha_0$ symmetry. Weak continuity conditions are nevertheless required to validate Fourier expansions. Nevertheless, these conditions are commonly satisfied for functions that indeed arise from statistical physics, as here the properties of the $\boldsymbol{c}$-director that is given by the average direction of the molecules, because they are generally expressed in terms of statistical integrals. So, the error that is committed relative to the real anchoring energy, when using Fourier expansions, remains somewhat independent of the actual value α_0 of the anchoring angle on the dislocation. Such a property is markedly different from the one-point convergence provided by the usual series [16]. Fourier series should therefore be favorably preferred to the one-point convergence series when we need a domain of large convergence radius.

The 1D anchoring energy of the $\boldsymbol{c}$-director onto an edge dislocation of Burgers vector unity can thus be expanded in a Fourier series up to the second order as $f_a^F = k_{a1} \cos\alpha_0 + k_{a2} \cos 2\alpha_0 + \cdots$. Let us recall that the sine terms in this Fourier expansion cancel because of the symmetry about $\boldsymbol{S}$, which warrants the angles $+\alpha_0$ and $-\alpha_0$ having the same energy.

For comparison, we try the two Fourier series reduced to the first and second orders, respectively,

$$f_a^{F1} = -k_{a1}^{F1} \cos\alpha_0 \tag{11}$$

and

$$f_a^{F2} = -k_{a1}^{F2} \cos\alpha_0 - k_{a2}^{F2} \cos 2\alpha_0, \tag{12}$$

where k_{a1}^{F1}, k_{a1}^{F2}, and k_{a2}^{F2} are the Fourier coefficients of the respective expansions.

These energy densities, i.e., per unit length of dislocation, are written in order to be minimal at $\alpha_0 = 0$ for positive anchoring constants. They can be simplified again on expanding them close to the equilibrium anchoring angle $\alpha_0 = 0$:

$$f_{a0}(\alpha_0) = \tfrac{1}{2} k_{a0} \, \alpha_0^2, \tag{13}$$

where α_0 is expressed in radians. This simple form was used in Ref. [6]. We try it again for comparison.

C. Torques exerted per unit length of dislocation

The derivatives of these anchoring energy densities yield the anchoring torques per unit length of dislocation according to their respective approximation. We can compare them to the experimental data,

$$\Gamma_a^{F1} = -k_{a1}^{F1} \sin\alpha_0, \tag{14}$$

$$\Gamma_a^{F2} = -k_{a1}^{F2} \sin\alpha_0 - 2k_{a2}^{F2} \sin 2\alpha_0, \tag{15}$$

in the first- and second-order Fourier series, respectively. The first-order expansion around $\alpha_0 = 0$ simply yields

$$\Gamma_{a0} = -k_{a0} \, \alpha_0. \tag{16}$$

Note that in this equation, the angle α_0 of the $\boldsymbol{c}$-director relative to the dislocation normal $\boldsymbol{S}$ is converted into radians to facilitate comparisons with the other expressions (14) and (15). Let us also notice that the anchoring torques, being restoring torques, are essentially negative. So, for convenience, we show them in Figs. 2 and 3 by means of their opposites.

Let us finally notice that, as Eq. (10) shows, the electric torque $\Gamma_E (\alpha_0)$ is regulated by general laws of physics and is therefore exactly calculable, while on the contrary, the anchoring torque $-\Gamma_a (\alpha_0)$ directly depends on the MHTAC molecule and on the chemical interactions that they exert with one another. We can therefore only know it through empirical functions of the anchoring angle α_0 that we fit on experimental data; cf. Eqs. (14)–(16). This makes a marked difference between them.
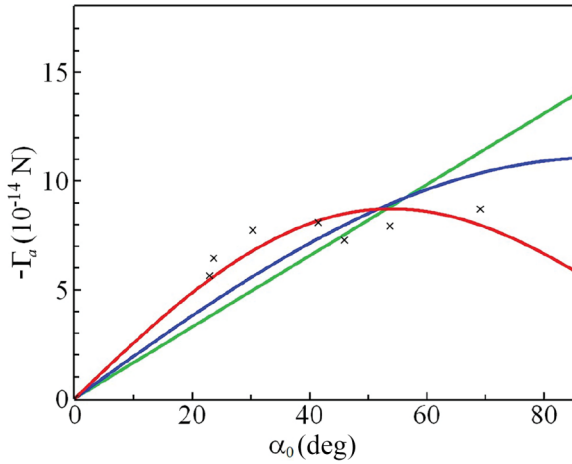
FIG. 2. Anchoring torque per unit length of edge dislocation, $-\Gamma_a$, exerted by the c-director on a dislocation line of Burgers vector, equal to the thickness of one smectic layer, l_{Sm}, vs its deviation angle α_0 on the dislocation. $-\Gamma_a$ is therefore measured in J/m, i.e., in N. This dislocation is observed at the interface of a SmC$_A$ film with $N = 72$ smectic layers and an isotropic puddle [Fig. 1(a)]. The experimental data are measured in the presence of an electric field E applied at an angle $\alpha_\infty = 116°$. The data are calculated exactly (black crosses) using Eq. (10). The green, blue, and red lines show the least-squares fits of the linear approximation, and the first- and second-order Fourier expansions, respectively.

III. DATA ANALYSIS

A. Experimental results

We can now test the above three expressions (14)–(16) of the anchoring torque versus the c-director angle onto the dislocation, α_0, upon fitting them to the experimental data of Ref. [6]. They have been obtained by measuring the orientation of the c-director on a dislocation as a function of an applied electric field, E, the c orientation being determined by means of the interference fringe observed under a crossed-polarizers microscope. These angular data allow one to recalculate exactly the applied electric torques by means of Eq. (10). In this manner, we avoid the linear approximations previously used for this calculation. So, the black crosses in Fig. 2 depict measured anchoring torques against the c-director angle on an edge dislocation, relative to the dislocation normal, S. Let us notice, too, that to avoid confusion, the cases that are dictated by the symmetry of the film structure to anchor in $\alpha_0 = 0°$ and $180°$ are omitted from Fig. 2. These points belong to the symmetry plane parallel to S. The anchoring energy in these places is therefore minimum or maximum, so that they correspond to stable or unstable equilibrium, respectively. Being continuous and derivable functions of the anchoring angle α_0, their derivatives, therefore, yield anchoring torques of zero value. Their coordinates are therefore (0,0) and (180°,0), respectively.

The green line in Fig. 2 shows the best fit of Eq. (16) on the experimental data. This is the first-order expansion of the anchoring torque close to $\alpha_0 = 0$, already used in Ref. [6]. As discussed above, its domain of validity is restricted, so that the fit is far from being satisfactory. Clearly, it divides the experimental data in two separate clusters, with an average
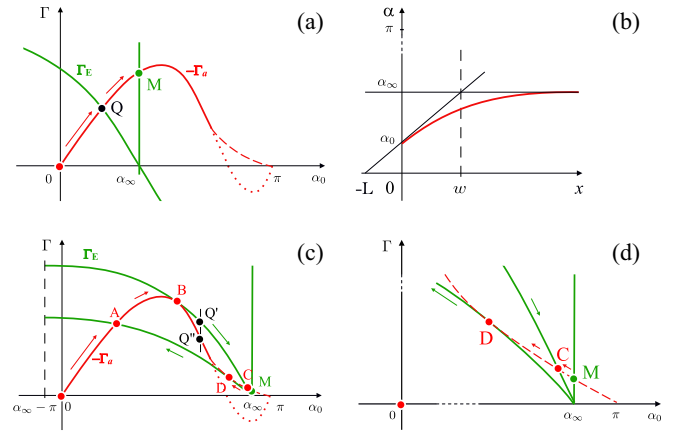

FIG. 3. (a), (c), and (d) Schematic routes followed by the operating point **Q** along reversible paths, and by its twins, **Q′** and **Q″**, along dissipative dual paths, respectively. The diagrams torque, Γ, vs anchoring angle on the edge dislocation, α_0, displays the electric (green) and anchoring (red) torques that drive the operating point as a function of α_0. Milestones **0**, **A**, **B**, **C**, **D**, and **M** mark strategic stages along the different routes. (a) Sketch of a one-intersection configuration between the $\Gamma_E(\alpha_0)$ and $-\Gamma_a(\alpha_0)$ lines in the case $\alpha_\infty < 130°$. (c) Three-intersection case for $130° < \alpha_\infty$. The twin operating points, **Q′** and **Q″**, follow the upper green arrow, along the dual dissipative paths, green and red, respectively (shown for increasing α_0). (d) Zoom by a factor of 3 of diagram (c) in the vicinity of α_∞. (b) Angle α of the c-director relative to S as a function of the distance x from edge dislocation.

standard deviation of about 2×10^{-14} N. The corresponding anchoring constant is $k_{a0} = 9.37 \times 10^{-14}$ N, or J per meter of dislocation, about twice the value found in the simplified analysis of Ref. [6], essentially because the calculation of the experimental torques is now done exactly on dropping the one-elastic-constant approximation, and on using the relative elastic anisotropy measured in the SmC$_A$ phase of the MHTAC compound, $\chi = 0.6$ [11].

The best fit of Eq. (14) on these data is depicted by the blue line (Fig. 2). This is the first-order Fourier expansion. Clearly, the fit is better than the linear, previous one. However, it shares again the data in two successive clusters in the figure, and its standard deviation, though lower, reaches 1.6×10^{-14} N. The anchoring constant that it yields is equal to the Fourier coefficient $k_{a1} = k_{a1}^{F1} = 11.07 \times 10^{-14}$ N. Clearly, though a little bit better, this Fourier expansion suffers by being limited to one term. This is clearly insufficient. We have to move to a second-order Fourier expansion.

The red line in Fig. 2 shows such a fit, Eq. (15), on the same experimental data. With a rather small standard deviation $\delta\Gamma_a = 0.9 \times 10^{-14}$ N, this fit clearly gives the best result, with the interesting property to *converge uniformly* over the whole experimental domain. In turn, this form needs two anchoring coefficients for describing the anchoring properties of the edge dislocation over an unusually large span of 180°. These two Fourier coefficients are $k_{a1}^{F2} = 5.07 \times 10^{-14}$ N and $k_{a2}^{F2} = 2.42 \times 10^{-14}$ N or again J per dislocation meter, respectively. They are indeed anchoring parameters that generalize the usual anchoring coefficient. A

relationship with it can be established in the domain of small anchoring angles. The second-order Fourier expansion is then approximated to a first-order expansion, only valid around $\alpha_0 = 0$. The corresponding anchoring constant is equal to $k_{a2} = k_{a1}^{F2} + 4k_{a2}^{F2} = 14.74 \times 10^{-14}$ N, a larger value, but in the same range as in the previous first-order evaluations, $k_{a0} = 9.37 \times 10^{-14}$ N and $k_{a1} = 11.07 \times 10^{-14}$ N. In this domain of relatively small anchoring angles, up to $\sim$1 rd, the standard deviation determined above, $\delta\Gamma_a = 0.9 \times 10^{-14}$ N, corresponds to an uncertainty in the angular measurements of about $\delta\alpha_0 \sim 5$ deg.

So, the average anchoring coefficient of the c-director on an edge dislocation line in a SmC_A film of MHTAC is found to be worth about $k_a^{1D} \sim 1.5 \times 10^{-13}$ N, where we have dropped the now useless subscript 2. This 1D anchoring coefficient, when multiplied by the rotation angle of the director α_0, written in radians, yields the torque that is applied per unit length of dislocation. To compare this value to known 2D anchoring coefficients, we have to convert this coefficient for two dimensions. Using the relation $k_a^{2D} = k_a^{1D} / l_{Sm}$, we deduce the equivalent 2D anchoring coefficient: $k_a^{2D} \sim 5 \times 10^{-5}$ J /m^2, which is the anchoring constant of a virtual 2D carpet of MHTAC molecules in the exact structure as in the edge dislocation core. Measurements of anchoring coefficients of nematic liquid crystals were obtained a long time ago on 2D solid surfaces. For homeotropic anchoring, i.e., with the director perpendicular to the surface, Yang *et al.* find $k_a^{2D} \sim 4.7 \times 10^{-5}$ J /m^2 [14], and for planar anchoring with pentyl-cyanobiphenyl (5CB) on SiO treatment, Yokoyama *et al.* obtain a similar result, $k_a^{2D} \sim 4 \times 10^{-5}$ J /m^2 [17]. Both results are consistent with the anchoring coefficient that we measure here on an edge dislocation line of a SmC_A film, though they were obtained with other molecules, in the nematic phase, and moreover were anchored on solid surfaces.

B. Total anchoring energy

From these results, we can calculate an order of magnitude of the anchoring energy required to reach the domain of large anchoring angles, where indeed the anchoring can potentially be broken. We estimate this order of magnitude from the difference between the minimum and the maximum anchoring energies for $\alpha_0 = 0$ and $\alpha_0 = \pi$ anchoring angles, respectively. As we see in Sec. IV B, they correspond to stable and unstable anchoring states. Their energy difference is $\Delta f_a^{F2} = f_a^{F2}(\alpha_0 = \pi) - f_a^{F2}(\alpha_0 = 0)$ per unit length of dislocation. From Eq. (12), we calculate that this energy amounts about to $\Delta f_a^{F2} = 2 k_{a1}^{F2} \sim 10^{-13}$ N. To appreciate the uncertainty made on this energy estimate, we start from the error that is done when measuring the torques. This uncertainty amounts about to $\delta\Gamma_a = 0.9 \times 10^{-14}$ N. It can then be transferred through Eqs. (15) and (12) to the anchoring coefficient k_{a1}^{F2} and then to the anchoring energies, which leads to $\delta f_a = 0.9 \times 10^{-14}$ N. This result is indeed valid independently of the Fourier analysis. We may thus drop the superscript $F2$ and simply write an approximate energy that the c-director spends after half a turn or a full rotation, on an edge dislocation: $\Delta f_a \sim 10^{-13} \pm 10^{-14}$ N, the anchoring angle then changing from $\alpha_0 = 0$ to $\alpha_0 = \pi$, or to $\alpha_0 = 2\pi$, respectively.

C. Partial melting of the edge dislocation core

The anchoring torque that an edge dislocation transmits to the smectic film is the addition of individual torques that come from MHTAC molecules inside the dislocation core. These torques themselves arise from energy variations of molecules in the core as a function of the c angle on the dislocation, $\alpha_0 = [S, c]$. We may thus anticipate that these torques are associated with small and progressive changes of molecule configurations in the edge-dislocation core when increasing α_0 from 0 to π. To simplify the discussion, we restrict our attention to core slices of thickness equal to the average lateral spacing between molecules, that is, about 1 nm. The core slice volume is then worth around 7 nm^3. With a molecule mass of 648 g, and taking into account that liquid crystal phases generally exhibit densities around 1, we estimate that the MHTAC molecules in the film occupy an individual average space of around 1 nm^3. The core slices therefore contain about seven molecules. While comparing both the cases where c is oriented parallel and antiparallel to S, as shown in Figs. 1(a) and 1(b), respectively, we may qualitatively understand the origin of the anchoring energy. Both the molecule organizations indeed differ in the step-edge region, inside the red circles of Figs. 1(a) and 1(b). The configuration is soft when the molecules are tilted in such a way as to soften the step edge; cf. Fig. 1(a). In the opposite case, where the molecules are mirrored about the **yz**-plane, perpendicular to the figure, the configuration is sharp, and the smectic phase enters like a horn inside the nematic phase; cf. Fig. 1(b). This geometric anomaly causes the prominent molecules in the smectic step edge to be swallowed in a nematic environment. This suggests that they should be destabilized and possibly melted at a microscopic scale. Such a mechanism of local and partial melting indeed costs an amount of energy that numerical modelings could help to estimate.

Nevertheless, we may evaluate the energy difference between the two, soft and sharp, configurations, based on the hypothesis that the anchoring energy is directly relevant to partial meltings in the dislocation core. The anchoring energies that exhibit the largest difference are reached for the two opposite c orientations relative to S, e.g., for $\alpha_0 = 0$ and $\alpha_0 = \pi$, respectively. They define the total anchoring energy that we have estimated in Sec. III B to be worth around $\Delta f_a \sim 10^{-13} \pm 10^{-14}$ J per dislocation meter, or equivalently, $\Delta f_a \sim 10^{-22}$ J/nm. At this stage, we may imagine two extreme molecule distributions in core slices of around seven molecules. In the first scenario, all the molecules carry about the same anchoring energy, that is, $\Delta f_a^{mol}(\pi) \sim 1.5 \times 10^{-23}$ J, or $\Delta f_a^{mol}(\pi) \sim 2.5 \times 10^{-3} k_B T$ per molecule in the dislocation core, where $k_B T \sim 6 \times 10^{-21}$ J, k_B being the Boltzmann constant and $T \sim 430$ K. In the second scenario, the core melting evoked above is mainly concentrated on one molecule, the most prominent one in the edge dislocation cliff, in the red circle of Fig. 1(b). Then, the anchoring energy carried by this molecule is about 10^{-22} J, or $1.5 \times 10^{-2} k_B T$. In both scenarios, the anchoring energies, supported by the most concerned molecules, remain two or three orders of magnitude below the thermodynamic energy per degree of freedom, $1/2 k_B T$. This shows that applying a torque to force an anchoring angle does not affect its molecular order nor its

structure enough to destabilize the dislocation, and eventually to melt it on macroscopic scales. Indeed, we have not observed such a large-scale melting. Naturally, these two extreme cases are schematic. The reality should be in between them, exhibiting a statistical melting in the step edge, with both space and time variations, i.e., with local gradients and intermittences.

To test which case could be the most realistic one, we can compare their local excess energy to the latent heat of a nematic–tilted smectic phase transition. A value $\Delta H \sim 0.4 \, \text{kcal/mol}$ was reported a long time ago for a nematic–smectic C phase transition in *p-n*-nonyloxy benzoic acid (NOBA), which corresponds to $\Delta H_{\text{mol}} \sim 2.7 \times 10^{-21}$ J per molecule, i.e., $\Delta H_{\text{mol}} \sim \frac{1}{2}k_B T$ [18]. The NOBA molecule has a similar length to MHTAC. Moreover, the tilted smectic is the SmC phase instead of SmC_A, but such a difference should not be decisive, and both the nematic–tilted smectic phase transitions should exhibit latent heats in the same range. So, the latent heat of nematic–tilted smectic phase transitions is much larger than the maximum anchoring energy by two or three orders of magnitude in any scenario. In the first scenario, where the anchoring energy is equally distributed over the dislocation core molecules, we thus have $\Delta f_a^{\text{mol}}(\pi) \sim 7 \times 10^{-3} \, \Delta H_{\text{mol}}$, and in the second one, where the whole anchoring energy is condensed on the most exposed molecule in the step cliff, we have $\Delta f_a^{\text{mol}}(\pi) \sim 5 \times 10^{-2} \, \Delta H_{\text{mol}}$. We therefore cannot conclude where to place the cursor between these two extreme scenarios. A numerical modeling could again be necessary to separate the two possibilities and to see which one is the most relevant.

IV. DISCUSSION

A. One-intersection case

1. Bell-shaped torque versus anchoring angle

As we immediately see from Fig. 2, the anchoring torque is not a linear function of the [S, c] angle on the dislocation, α_0. The red line that depicts $-\Gamma_a(\alpha_0)$, the least-squares fit of the second-order Fourier expansion on the experimental data, exhibits a maximum in the available range. The coordinates of this maximum are readily extracted from Eq. (15): $-\Gamma_a^{\text{max}} = 8.7 \times 10^{-14} N$ at $\alpha_0^{\text{max}} \sim 54°$. From this summit, the anchoring torque decreases towards zero. The anchoring torque $-\Gamma_a$ is null at $\alpha_0 = 0$ and seems to do the same in $\alpha_0 = \pi$ (rd). These zero values of α_0 are indeed consistent with the symmetry of the film structure about S, as discussed in Sec. III. When no electric field E is applied, these anchoring angles correspond to stable and unstable *equilibria*, respectively.

Indeed, the Fourier analysis provides interesting indications, but it can also add flaws. Before reaching the last point at $\alpha_0 = \pi$, the anchoring torque $-\Gamma_a(\alpha_0)$, given by Eq. (15), makes an oscillation that is relevant to a Fourier series truncation at the second order [Fig. 3(a)]. Such a negative oscillation of amplitude around the order of magnitude of the experimental error is indeed artificial. All along this oscillation, close to $\alpha_0 = \pi$, the anchoring torque seems to become positive, with a c-director attraction towards the $-S$ direction, which is opposite to its initial attraction towards S. Such a behavior has indeed no physical explanation and must be considered illusory. We therefore mark the dubious track with dots in

Figs. 3(a) and 3(c). Instead, we propose a more realistic behavior in the form of a simple and direct extrapolation towards the point of coordinates ($\alpha_0 = 180°$, $-\Gamma_a = 0$), and depicted with a red dashed line. Clearly, detailed measurements should be necessary to ascertain this point. Such additional data could also allow for the determination of higher-order terms in the Fourier series expansion, and for a reduction of the amplitude and period of the parasitic oscillations, until they definitely vanish into the experimental noise.

2. Linear approximations

Figure 3(a) sketches the torque variations versus the anchoring angle α_0 according to Eq. (15) in the case $\alpha_\infty \sim 116°$, which corresponds to the experimental results of Fig. 2. In the vicinity of $\alpha_0 = 0$, far from maximum, the anchoring torque $-\Gamma_a(\alpha_0)$ exhibits linear variations. The calculations can then be simplified by using the one-elastic-constant approximation, and by choosing the elastic anisotropy $\chi = 0$ again. These simplifications are helpful for a better understanding of particular features in the c anchoring on edge dislocations. Equations (7) and (10) then become, respectively,

$$\frac{\partial \alpha}{\partial x} = \frac{2}{w} \sin\left(\frac{\alpha_\infty - \alpha}{2}\right) \tag{17}$$

and

$$\Gamma_E = 2\sqrt{PEK} \int_{\alpha_0}^{\alpha_\infty} \cos\left(\frac{\alpha_\infty - \alpha}{2}\right) d\alpha. \tag{18}$$

This last equation can easily be integrated to

$$\Gamma_E = 4\sqrt{PEK} \, \sin\left(\frac{\alpha_\infty - \alpha_0}{2}\right). \tag{19}$$

We naturally restrict the calculations to the cases where both α_0 and $\alpha_\infty - \alpha_0$ are significantly smaller than 1 rd. Such an approximation allows us to express Eqs. (17) and (19), respectively, as

$$\alpha - \alpha_\infty = (\alpha_0 - \alpha_\infty) \exp\left(-\frac{x}{w}\right) \tag{20}$$

and

$$\Gamma_E = 2\sqrt{PEK}(\alpha_\infty - \alpha_0). \tag{21}$$

Equation (20) is written for the $x > 0$ region only. The $x < 0$ part can be deduced by symmetry, or simply by changing x in $|x|$.

The variations of the angle α that the c-director makes relative to S as a function of distance x to the dislocation are sketched in Fig. 3(b) according to Eq. (20) in the case of small α_∞, i.e., again, for $\alpha_\infty < 1$ rd. This graph illustrates the role of two characteristic distances in the anchoring problem, namely the distortion distance and the extrapolation length, w and L, respectively,

$$w = \sqrt{\frac{K}{PE}}$$

$$L = \frac{2K}{k_a}, \tag{22}$$

where $k_a = 1.5 \times 10^{-13}$ N, cf. Sec. III A. Let us notice that the anchoring torque of coefficient k_a acts on both sides of the dislocation line, that is, on two half-spaces. The anchoring torque

that the line transmits to each side of the film and that basically enters in the extrapolation length expression is therefore one-half of the total anchoring torque. This k_a value allows us to estimate the extrapolation length $L = N \times 10^{-7}$ m, which is worth $L = 7.2\,\mu$m in the present experiment where $N = 72$. The extrapolation length, though larger than usual, nevertheless remains smaller than the wall width, $w = \sqrt{N} \times 2.2\,\mu$m, that is, $w_{160} = 14.7\,\mu$m for a voltage $V = 160$ V applied on a 72-layer film.

In order not to mix the effect that arises from the film thickness with the anchoring property of edge dislocations, we introduce the intrinsic extrapolation length of a one-smectic-layer-thick film, i.e., where $N = 1$. The intrinsic extrapolation length of MHTAC films can then be defined as $L_1 = L/N = 100$ nm. This value compares well with the value $L = 125$ nm measured by Yokoyama *et al.* for pentyl-cyano-biphenyl (5CB) on obliquely evaporated SiO [17]. Measurements performed on polymer surfaces yield weaker anchorings and therefore larger extrapolation lengths. So, with rubbed polyimide and nylon films, extrapolation lengths are measured to be 330 nm [19] and 450 nm [20], respectively.

3. Amplification factor

Coming back to the anchoring of a 72-layer film on an edge dislocation, we see that this special junction leads to an effective extrapolation length almost two orders of magnitude larger than in usual nematic anchorings. This indeed means an extraordinarily weak anchoring that seems able to provide an amplification of the anchoring effects. However, the actually measured quantity is indeed the anchoring angle on the dislocation, α_0, instead of the extrapolation length itself, L.

Equations (16) and (20) that are valid for small α_∞ values lead to a simple expression of α_0 as a function of α_∞, when combined with the equilibrium relation (8):

$$\alpha_0 = \frac{\alpha_\infty}{1 + \frac{w}{L}}. \tag{23}$$

This equation shows that the key parameter that governs the c anchoring on a dislocation is the ratio between the extrapolation and distortion lengths, which is expressed as

$$\frac{L}{w} = 2\frac{\sqrt{KPE}}{k_a}. \tag{24}$$

This ratio, extrapolation over distortion lengths, is proportional to $\sqrt{KPE} \sim \sqrt{EN}$, which shows that it is easy to change the anchoring conditions just by acting on the film thickness, $N\,l_{\mathrm{Sm}}$, or more readily, by changing the modulus of the electric field, E. Reversing the sign of $\boldsymbol{E}$ is also a third possibility as this leads to replace α_∞ by $\pi - \alpha_\infty$; cf. Sec. IV A 5. In practice, however, films thicker than $N > 500$ are not stable enough to perform correct measurements. We therefore do not have a real access to this thick-film domain. Equation (24) indeed indicates that we are practically limited to cases where the ratio L/w is smaller than 1. So, the anchoring angle on an edge dislocation increases roughly as

$$\alpha_0 \sim \frac{L}{w} \sim \sqrt{N}. \tag{25}$$

This N dependence, shown by means of linear approximations here, evidences a useful *amplification factor* of α_0

that should be valid when both α_0 and α_∞ are smaller than 1 rd. For larger angles, this amplification factor will only be approximate.

4. Approximation $\chi = 0$

As Eq. (10) shows, the anchoring angle α_0 is a key parameter that allows us to calculate the applied electric torque exactly, and to deduce the anchoring torque at equilibrium. The experimental determination of α_0 is consequently decisive, and it has to be performed as accurately as possible. Equation (10) moreover shows that the electric torque Γ_E that the smectic film exerts on an edge dislocation is proportional to the factor $F = \sqrt{EN}\,I(\alpha_\infty, \alpha_0, \chi)$, where $I(\alpha_\infty, \alpha_0, \chi)$ stands for the integral in Eq. (10). So all in all, the factor F evidences that the electric control of the film is determined by the applied voltage V, by the film thickness, $N\,l_{\mathrm{Sm}}$, and by the angle, α_∞, of the electric field $\boldsymbol{E}$ relative to the dislocation normal $\boldsymbol{S}$; cf. Sec. IV A 5. With the assumption $\chi = 0$, it simplifies to $I(\alpha_\infty, \alpha_0, \chi = 0) = 2\sin(\frac{\alpha_\infty - \alpha_0}{2})$. Moreover, the factor F shows that the electric torque functions $\Gamma_E(\alpha_0)$ are exactly proportional to one another when they are calculated for different voltages, provided that the electric field angle, α_∞, stays the same. We shall make use of this theorem to draw and discuss Figs. 3(a), 3(c), and 3(d) below.

Numerical calculations of the ratio $R_\chi = I(\alpha_\infty, \alpha_0, \chi)/I(\alpha_\infty, \alpha_0, \chi = 0)$ show that R_χ stays roughly stable over a wide range. We thus approximately find that $R_\chi \sim 1.1 \pm 0.08$ for $\alpha_0 < 60°$ in the first interval $\alpha_\infty < 90°$. Here, ± 0.08 stands for R_χ variations as a function of α_0. These variations, therefore, express a distortion of $I(\alpha_\infty, \alpha_0, \chi)$ relative to the sine function in $I(\alpha_\infty, \alpha_0, \chi = 0)$. Similarly, in the next interval $110° < \alpha_\infty < 150°$, we calculate $R_\chi \sim 1.07 \pm 0.08$ for $\alpha_0 < 120°$, and in the last interval $150 < \alpha_\infty < 180°$, $R_\chi \sim 0.97 \pm 0.08$ for $\alpha_0 < 120°$. So, R_χ exhibits average values that slightly vary around 1 according to the α_∞ choice. These slight variations only change the overall proportionality factor F that enters in the electric torque expression, $\Gamma_E(\alpha_0)$, without producing distortions in $\Gamma_E(\alpha_0)$. However, small distortions superimpose because of the fluctuations that appear when calculating different R_χ as a function of α_0 for the same α_∞ value. They are on the order of 8%. So, for qualitative analyses, we may indeed approximate the proportionality factor F with the relation $F \sim 2\sqrt{EN}\,\sin(\frac{\alpha_\infty - \alpha_0}{2})$. This comes to express the electric torque $\Gamma_E(\alpha_0)$ by means of Eq. (19) instead of Eq. (10), with, however, a supplementary multiplicative term between 0.95 and 1.10 according to the value of α_∞.

5. Three experimental parameters

Practically, the film thickness is determined at the beginning of the experiment when preparing an induced smectic film on an isotropic MHTAC puddle. The last parameter α_∞ is fixed when selecting the dislocation line to be studied on the film, and when choosing the sign of the voltage that we apply on the electrodes. Changing the voltage sign comes to subtract π from α_∞. If we then apply a symmetry around the dislocation normal, $\boldsymbol{S}$, which is equivalent to changing the sign of the angles, the initial α_∞ angle becomes $\pi - \alpha_\infty$. So,

provided that we use voltage sign changes, we can adjust α_∞ to a large span of values inside the $[0, \pi]$ range. These three parameters—the applied voltage V, N, and α_∞—thus yield the useful experimental means to choose the torque $\Gamma_E (\alpha_0)$ to apply on a dislocation, cf. Sec. IV A 4, and therefore for measuring the anchoring properties of the *c*-director on it. In particular, when we increase E from 0 to large values, α_0 goes from 0 to α_∞. Naturally, when α_0 gets close to α_∞, we need to increase E some more to compensate for the consecutive decrease of the $\alpha_\infty - \alpha_0$ difference. Moreover, the whole process takes time. We then need some luck for the dislocation to remain steady enough in the microscope field, and therefore for the layer number N to remain constant, too.

6. Reversibility

At this stage, we may observe two different situations. In the simplest one, the two lines that represent the torques $\Gamma_E (\alpha_0)$ and $-\Gamma_a (\alpha_0)$ exhibit only one intersection at a point **Q** in the range $[0, \alpha_\infty]$; cf. Fig. 3(a). **Q** is indeed the *operating point* that represents the *c*-director anchoring on the edge dislocation. When we increase the applied voltage and thus the electric field E, the factor F increases monotonically, too, from 0 to infinity; cf. Sec. IV A 4. Meanwhile, the electric torque $\Gamma_E (\alpha_0)$ increases, as also the abscissa of point **Q**, α_0, that gradually goes from $\alpha_0 = 0$ until reaching α_∞ for infinite E. Then, **Q** moves from **0** to **M**. However, because of viscosity, the process could take a long time. So practically, we increase the voltage by steps of a few volts, waiting one or two minutes for a new equilibrium. Such a one-intersection behavior obviously obeys a linear regime in the interval $0 < \alpha_0 < 45°$. For larger α_0 values, the two functions $\Gamma_E (\alpha_0)$ and $-\Gamma_a (\alpha_0)$ begin to exhibit curvatures, but fortunately the $\Gamma_E (\alpha_0)$ curvature is weak, so that both functions continue to exhibit only one intersection, provided that $\alpha_\infty < 130°$. These features are indeed consistent with the experimental results analyzed in Fig. 2, where we have $\alpha_\infty = 116°$.

We then decrease E from infinity back to 0 while proceeding in steps and waiting each time for equilibrium, as when increasing E from 0 on the forward path. Thus, while decreasing α_0 from α_∞ to 0, the operating point **Q** goes back to **0** from **M** on the same path **[0,M]** but by going in the opposite direction. A complete back and forth process along a single track is thus observed in the cases where $\alpha_\infty < 130°$, provided that we go reversibly, by waiting long enough for quasiequilibrium after each step. We can also verify under a polarizing microscope that the interference fringe remains fluid and able to move reversibly inside the entire angular domain, which indeed indicates that **Q** has not yet reached any broken anchoring state.

B. Irreversible process in a 2D liquid

Naturally, linear approximations of both the torques are not correct far from $\alpha_0 = 0$, and Eqs. (16) and (21) cannot be used anymore. Numerical calculations should then be undertaken to catch the exact values of the electric and anchoring torques, $\Gamma_E (\alpha_0)$ and $-\Gamma_a (\alpha_0)$, in particular in the three-intersection case, i.e., in the domain $130° < \alpha_\infty$. Nevertheless, we can discuss some anchoring properties in the domain $130° < \alpha_\infty$ by means of the anchoring torque data $-\Gamma_a (\alpha_0)$ that were already obtained in the $\alpha_\infty < 130°$ domain, since they indeed are intrinsic and independent of the α_∞ value. Moreover, exact calculations may be avoided when we just intend to understand the manner in which these lines move relative to each other, in particular, when we are interested in the transition between the two configurations where the electric and anchoring torque functions intersect in one and three places, respectively; cf. Sec. IV A 4. At this transition, the lines are just tangent to each other.

1. Three-intersection case

So, let us consider the domain $130° < \alpha_\infty$. We begin with $F = 0$ and we gradually increase this parameter by small voltage steps. Thus, $\Gamma_E (\alpha_0)$ increases proportionally and its movement shifts the abscissa of its intersection with $-\Gamma_a (\alpha_0)$ (red arrows) towards larger values. Finally, α_0 passes over the bell summit around $\alpha_0^{max} \sim 54°$, until both lines $\Gamma_E (\alpha_0)$ and $-\Gamma_a (\alpha_0)$ get tangent to each other in point **B**, a little bit farther than the maximum; cf. Fig. 3(c). Then, the voltage is worth about $V = 160$ V and $E = 8 \times 10^4$ V m^{-1}. Naturally, at this milestone point, the electric and the anchoring torques Γ_E and $-\Gamma_a$ are equal, so that if we increase E again, the two lines separate from each other. The equilibrium is then broken, and Γ_E, being larger than $-\Gamma_a$, definitely drives the *c*-director to get almost parallel to $\boldsymbol{E}$, and consequently α_0 becomes closer to α_∞ (green arrow). At the same time, because $\Gamma_E (\alpha_0)$ and $-\Gamma_a (\alpha_0)$ are different, the operating point **Q** splits in twin operating points **Q′** and **Q″** of common abscissa α_0 that *freely* travel along their green and red lines, respectively. The movement stops when the operating point **Q** finds a new equilibrium in a new milestone point, **C**, at the intersection between the lines $\Gamma_E (\alpha_0)$ and $-\Gamma_a (\alpha_0)$. This milestone **C** marks the end of the free out-of-equilibrium travel of both **Q′** and **Q″** along the dual path **BC**. This travel is performed freely, i.e., at a constant voltage close to 160 V, without needing successive voltage steps with intermediate equilibrium stages. Thus, the anchoring evolves in an out-of-equilibrium and irreversible manner. Moreover, the **Q** separation in twin operating points **Q′** and **Q″** of common abscissa α_0 evidences that the electric and anchoring torques are unequal now, and that their difference corresponds to a viscous torque, as detailed in Sec. IV B 2. The viscous torque hinders the **c**-rotation and dissipates its energy over the 3D volume of the film in w wide ribbons along both sides of the dislocation, for a total width of $2w$. Typical values of w are in the range ~ 10–20 μm depending on voltage. This dissipated energy can be measured from the area between the red and green **BC** paths that the $\Gamma_E (\alpha_0)$ and $-\Gamma_a (\alpha_0)$ torques follow, respectively. The dissipated energy that **Q** spends along its **BC** paths measures the degree of irreversibility of its movement.

Irreversible processes in physics are generally considered to be specific to solids. As we can see here, this is not always the case. Moreover, our system, when restricted to the plane of the smectic layers, may be considered a *perfect 2D liquid*, provided that the film is free of defects except for the dislocation on which we measure the *c*-director anchoring. Nevertheless, it is not an ordinary liquid, but a liquid crystal, with therefore some solidlike properties; see below. Being made of a tilted smectic phase, the film carries an orientational order which

indeed explains the existence of dissipation and irreversible processes. Interestingly too, this orientational order allows one to realize a rotating *two-state lock* that jumps from a low- or middle-range α_0 angle, between **0** and **B**, to a large α_0 angle, close to α_∞, between **C** and **D**, respectively; see Sec. IV C 3. The command of the lock is provided by the electric field, which is able to move it from one anchoring state to the other.

2. Dissipation work

Let us now detail some irreversible properties that are initiated from point **B** on the way to point **C**. For this purpose, qualitative handmade graphs such as Figs. 3(c) and 3(d) are helpful. Belonging to the three-intersection cases, α_∞ is larger than $130°$, rather close to π, and kept constant during the whole film measurements. While progressively increasing α_0 from 0, i.e., by increasing the electric field E, the electric and anchoring torques $\Gamma_E(\alpha_0)$ and $-\Gamma_a(\alpha_0)$ remain equal to each other, at equilibrium, before reaching point **B**. At this point, as mentioned above, the voltage is approximately equal to 160 V. Slightly increasing the voltage again causes the lines $\Gamma_E(\alpha_0)$ and $-\Gamma_a(\alpha_0)$ to separate. This means that the sum $\Gamma_E(\alpha_0) + \Gamma_a(\alpha_0)$ is no longer zero, and that the equilibrium is broken. As a result, the operating point **Q** exceptionally divides into twin points **Q′** and **Q″** of common abscissa α_0, as mentioned in the previous section. They follow electric and anchoring paths, green and red, respectively, so that Eq. (8) becomes

$$\Gamma_E + \Gamma_a = \Gamma_{\text{visc}} = \int_{\text{film}} \Gamma_{\text{visc}}^{\text{local}} \, dV, \qquad (26)$$

where $\Gamma_{\text{visc}}^{\text{local}} = \gamma_1 \frac{\partial \alpha}{\partial t} N \, l_{\text{Sm}}$ stands for the local viscous torque that hinders the azimuthal rotations of the **c**-director around the **z**-axis. Their viscosity coefficient is indeed different from the viscosity coefficient related to tilt fluctuations. Integrating Eq. (26) over the film volume yields the viscous, or dissipative, torque Γ_{visc} that the edge dislocation receives from the smectic film per unit length:

$$\Gamma_{\text{visc}} = 2 \int_0^\infty \gamma_1 N \, l_{\text{Sm}} \frac{\partial \alpha}{\partial t} \, dx, \qquad (27)$$

the factor of 2 standing for the two parts of the film on both sides of the dislocation. The voltage being kept constant after point **B**, we deduce $\frac{\partial \alpha}{\partial t} = \frac{\partial \alpha_0(t)}{\partial t} \exp(-\frac{x}{w_{160}})$ from Eq. (20), and we estimate

$$\Gamma_{\text{visc}}(\alpha_0) = 2\gamma_1 N \, l_{\text{Sm}} \int_0^\infty \frac{\partial \alpha_0}{\partial t} \exp\left(-\frac{x}{w_{160}}\right) dx$$
$$= Y_{160} \frac{\partial \alpha_0}{\partial t}, \qquad (28)$$

with

$$Y_{160} = 2\gamma_1 N \, l_{\text{Sm}} \, w_{160}. \qquad (29)$$

The second member of Eq. (26) is the viscous torque, which can be expressed in a shorter form, Eqs. (28) and (29), where $w_{160} = 14.7 \, \mu\text{m}$ is the wall width for a voltage $V = 160 \, \text{V}$. To complete the calculation of the dissipation work, we need to recall estimates of the rotational viscosity γ_1 in different tilted smectics. Indeed, this coefficient

has been determined in a SmC liquid crystal, di-(4-n-decyloxybenzal)-2-chloro-l-4-phenylene diamine (DOBCP), which yields $\gamma_1 \sim 0.06 \, \text{Pa s}$, a probably overestimated value as the measurement has been performed about $10 \, °\text{C}$ below the smectic-C to nematic transition, while we need viscosity values close to the isotropic phase [21]. Other values have been reported on different compounds. They yield $\gamma_1 \sim 0.02 \, \text{Pa s}$ in di-n-heptyloxyazoxybenzene (DHAB) [22]. Somewhat smaller values are obtained, $\gamma_1 \sim 0.004 \, \text{Pa s}$ in p-n-decyloxybenzylidene-p'-amino-2-methyl-butyl-cinnamate (DOBAMBC) and $\gamma_1 \sim 0.006 \, \text{Pa s}$ in p-decyloxibenzilidene-p'-amino-1-methylpropyl-cinnamate (DOBA1MPC) [23], and in compounds that belong to the [2S,3S]-4-(2-chloro-4-methylpentanoy1oxy)phenyl *trans*-4″-n-alkoxy cinnamate series [24]. These last measurements show that γ_1 increases for molecules with short alkyl chains. With our MHTAC molecule exhibiting a somewhat shorter aliphatic tail than the molecules in the above references, we may anticipate an average rotational viscosity of $\gamma_1 \sim 0.01 \, \text{Pa s}$. Nevertheless, as evidenced from Ref. [23], changes in the chemical structure of the molecules have larger effects on the viscosity than the length of alkyl chains. This value of $\gamma_1 \sim 0.01 \, \text{Pa s}$ should therefore be understood as a rough estimate of the viscosity, with perhaps an uncertainty factor of 1.5–2. Nevertheless, without any measurement of the MHTAC viscosity, we keep this value to estimate $Y_{160} \sim 10^{-13} \, \text{J}$, and to evaluate the dissipation work that the operating point **Q** spends when traveling along a $\delta\alpha_0$ viscous path under an applied voltage of 160 V, with the expression

$$\delta W(\alpha_0) = \Gamma_{\text{visc}}(\alpha_0)\delta\alpha_0 = Y_{160} \frac{(\delta\alpha_0)^2}{\delta t}. \qquad (30)$$

3. Travel time along a reversible path

Along the branch **0AB**, the interference fringe that is observed under the polarizing microscope exhibits easy fluidity and free reversibility when the film is submitted to voltage variations. Indeed, its response appears to be immediate in one direction or the opposite one, according to the sign of the E variations. However, this observation needs to be detailed further. Indeed, Eq. (30) may be used to tentatively estimate the time that the operating point **Q** needs to travel, for instance, from **0** to **A**. This time can be expressed in terms of the viscous torque $\delta\Gamma(\alpha_0) = \Gamma_E(\alpha_0) + \Gamma_a(\alpha_0)$ by means of the integration of Eq. (30):

$$\tau_{0A} \sim Y_{160} \int_0^{\alpha_A} \frac{d\alpha_0}{\delta\Gamma(\alpha_0)}. \qquad (31)$$

If the path **0A** is followed reversibly, i.e., while respecting an almost permanent equilibrium throughout, negligible dissipation should occur. The denominator of the fraction should then be close to zero, but then Eq. (31) diverges, which is physically unacceptable, as the **Q** trip from **0** to **A** would take an infinite time. In fact, the sum of the torques applied on the dislocation, $\delta\Gamma$, cannot be exactly zero. Experimentally, we are only able to keep $\delta\Gamma$ within the torque error bar observed in the measurements, an error bar that incidentally corresponds to about six times the thickness of the red or green lines in Fig. 3(c). Therefore, the condition on the viscous

torque $\delta\Gamma = \Gamma_E(\alpha_0) + \Gamma_a(\alpha_0) \leqslant 0.9 \times 10^{-14}$ N is necessary but also sufficient, as it is experimentally equivalent to the zero condition. So, the operating point **Q** that moves along the reversible path **0AB** is supposed to be in *quasiequilibrium* as long as **Q** stays within the resolution limit. This experimental point of view has two direct advantages: first, the divergence has formally disappeared, and second, the running time of **Q** along the **0AB** path is now experimentally acceptable. To estimate this travel time, we need to detail the manner in which we tune the electric field E.

Practically, it is difficult to increase E while keeping the viscous torque $\delta\Gamma$ continuously inside the error limit. So, we proceed in an easier manner, already described in Sec. IV A 6. We regularly increase the voltage along the reversible paths, similar to the path from **0** to **A**, by steps of about 3–5 V followed by an equilibrium time. As Fig. 3(c) shows, this path **0A** belongs to an α_0 range where $-\Gamma_a(\alpha_0)$ can be replaced by linear approximations; cf. Sec. IV A 2. The electric torque $\Gamma_E(\alpha_0)$ behaves differently, and exhibits quasi-sine and exact quadratic variations relative to α_0 and to E, respectively; cf. Sec. IV A 4. Practically, the electric torque function can be reduced to the relation $\Gamma_E \sim \sqrt{E}$. This indicates that the $\Gamma_E(\alpha_0)$ variations in point **A** are similar to the $\Gamma_E(\alpha_0)$ variations in point **B**, with a proportionality reduction of $\sim 50\%$; cf. Fig. 3(c). So conversely, the voltage in **A** corresponds to the voltage in **B** with a reduction factor of 4. Point **B** being close to the bell summit, its voltage is worth about $V = 160$ V, and therefore the voltage in **A** is about equal to 40 V. We can now calibrate the torque step value to respect the reversibility condition along path **0A**. As discussed above, the $\delta\Gamma_E$ steps should stay below the error bar $\delta\Gamma \sim 0.9 \times 10^{-14}$ N, which roughly corresponds to $\delta\alpha_0 \sim 0.08$ rd or 5 degrees when converted along the linear **0A** path. This angular error bar then extends to the whole angular range, as the uncertainties of measurements are indeed the same over the whole angular range. From this error bar, we can deduce the size of the V steps by using the derivative of the expression $\Gamma_E \sim \sqrt{E}$. Because of their quadratic variations, the V steps depend on the location of point **Q** in Fig. 3(c). They are

$$\delta V = 2 \times V \, \frac{\delta\Gamma_E}{\Gamma_E}. \tag{32}$$

In the vicinity of point **A**, they should be smaller than $\delta V \sim 7$ V. In practice, we take $\delta V \sim 5$ V, but possibly with shortened waiting times for equilibrium. With these figures, Eq. (31) yields an average time per step $\Delta\tau \sim 10$ s, which leads to a total time $\tau_{0A} \sim 1.5$ mn for the **0A** path, a practical evaluation that is consistent with the experimental observations. Let us also notice that this estimate justifies *a posteriori* a measurement process that indeed uses gliding steps. Experimentally, such a process consists in anticipating the moment to make the next step, since we cannot really observe the interference fringe stabilization as soon as its center displacement falls below the angular resolution, $\delta\alpha_0 \sim 5$ degrees.

In summary, the more we comply with a careful equilibrium along a reversible path, the longer it takes. Such an assertion indeed seems evident. Nevertheless, as shown above, the experimental reversibility condition is not very demanding as we can choose a process implying successive and not too small steps, each one with an amplitude staying inside the

error bars. According to the above estimates, the travel time over the whole **0B** path should thus take about 3 mn, again consistent with the observations.

4. Dissipative path

When the operating point **Q** passes milestone **B** while increasing α_0, indeed **Q** splits into twin points **Q′** and **Q″** that travel along the green and red lines, respectively; cf. Sec. IV B 1. At this moment, $\Gamma_E(\alpha_0)$ becomes larger than $-\Gamma_a(\alpha_0)$. The viscous torque $\delta\Gamma = \Gamma_E + \Gamma_a$ is then positive and drives α_0 towards **C**. Because the viscosity is involved in the process, cf. Eq. (26), the path **BC** is now dissipative and irreversible. In principle, **Q** should not need any more help to spontaneously move towards **C**. However, at the beginning of the path starting from **B**, the viscous torque $\delta\Gamma$ is small and remains below the error bar until reaching the abscissa $\alpha_0(B+) = \alpha_0(B) + \delta\alpha_0$, where $\delta\alpha_0 \sim 5$ degrees. There, point **B+** is already broken up into twin points **B+′** and **B+″** that are located close to the middle of paths **BQ′** and **BQ″**, respectively [Fig. 3(c)]. However, as along the reversible path **0B**, the viscous torque is again insufficient to push **Q** towards **B+** in a reasonable time. We thus have to increase the voltage again by successive steps as we did along path **0B**. As shown in Sec. IV B 3, each step should last about $\Delta\tau \sim 10$ s.

Indeed, points **B** and **C** mark the beginning and end of the anchoring breaking process, respectively; see details in Sec. IV C.

5. Free flight of a few seconds

From **B+** towards **C,** the viscous torque is larger than $\delta\Gamma$, so it is no longer necessary to increase the voltage to push the operating point **Q** towards **C**. However, in the vicinity of **C**, the problem is somehow similar to the one encountered close to **B**. After the abscissa $\alpha_0(C-) = \alpha_0(C) - \delta\alpha_0$ of both the points **C−′** and **C−″**, the operating point **Q** enters a small viscous torque domain where it is necessary again to push **Q** by increasing the voltage. So, **Q** freely moves between these two limits, $\alpha_0(B+)$ and $\alpha_0(C-)$. We can then estimate an upper bound for the free flight time between **B+** and **C−**. The relation $\delta\Gamma(\alpha_0) > 0.9 \times 10^{-14}$ N being satisfied all along the trip between **B+** and **C−**, we deduce from Eq. (31) that the flight time from **B+** to **C−** obeys the inequality $\tau_{BC} < Y_{160} \int_B^C \frac{d\alpha_0}{0.9 \times 10^{-14}}$, where the $+$ and $-$ signs have been dropped for simplicity. We thus deduce that $\tau_{BC} < 10$ s, a short time of flight that contrasts with the longer times that were necessary along the previous, reversible paths. In addition, we can anticipate that the actual time to run from **B+** to **C−** should indeed be shorter by a factor of about 2, i.e., $\tau_{BC} \sim 5$ s, as $\delta\Gamma$ is clearly larger everywhere than its minimum of 0.9×10^{-14} N that we use for this estimate. This short time is somehow the signature of the irreversible process that is initiated in point **B**. Such a feature is just opposite to the behavior observed in infinitely slow reversible processes. This time estimate is also consistent with the surprisingly fast displacement of the interference fringe that we have observed at this moment under the microscope, in clear contrast with the inertia that the fringe demonstrates along path **0B**.

6. Difficult access to milestone C

However, an important difference exists between milestones **B** and **C**. Passing point **B** is easy. We just have to push the operating point **Q** by means of weak voltage steps, of $\delta V \sim 5$ V. From Fig. 3(d), which depicts a part of Fig. 3(c) zoomed by a factor of about 3, we can estimate that the torque uncertainty is worth about $\delta\Gamma \sim \Gamma(\mathbf{C})$. From Eq. (32), and recalling that the voltage at points **B** and **C** is about 160 V, we deduce that we need voltage steps of amplitude $\delta V = 2 \times V \times \delta\Gamma/\Gamma(\mathbf{C}) \sim 2 \times 160 = 320$ V to push point **Q** forward in order to pass milestone **C**. Indeed, we may need to apply up to our maximum voltage of 500 V, and even more if a first step is insufficient. As discussed in Sec. IV D, films induced on isotropic puddles become too unstable to allow us to perform correct measurements in the range $130° < \alpha_\infty$. Essentially, large electric fields favor the nucleation of high Burgers vector dislocations that may suddenly invade the whole film, causing the film thickness to increase to unknown numbers of layers. For this reason, we could only make quick observations around the passage of milestone **C**. Additionally, reproducing the observation needed to relaunch point **Q** from **B** again, but with point **C** working as a valve, see Sec. IV C 2, required **Q** to pass through point **A** again. Clearly, such a complication takes a long time with a serious risk of final film destabilization.

C. Breaking of the anchoring

For the operating point **Q** to effectively pass **C**, which we observed only a few times, we had to increase the factor F to its maximum available value by applying our highest voltage of 500 V. $\Gamma_E (\alpha_0)$ then tends to become a steep line; cf. Fig. 3(d). This line, though not perfectly vertical, intersects $-\Gamma_a (\alpha_0)$ at the abscissa α_∞, slightly past the terminal milestone **M**.

1. Complete breaking of the anchoring

After point **Q** passes through milestone **B**, the anchoring is broken. Point **Q** then goes through milestone **C** before finally arriving close to milestone **M**. During this process, the c-director on the dislocation becomes almost aligned along the electric field $\mathbf{E}$, with the anchoring angle α_0 becoming about equal to α_∞. This demonstrates that the dislocation now has a negligible effect on c. This decoupling between c and $\mathbf{S}$ confirms, if necessary, that the dislocation anchoring is broken. Moreover, α_∞ being the maximum abscissa that α_0 can reach, **M** is also a border marker for the operating point **Q** in the $-\Gamma_a (\alpha_0)$ graph. It is worth noting that the milestones **A**, **B**, **C**, **D**, and **M** are indeed functions of α_∞. This is clear for **M** [Fig. 3(d)], but also for **A**, **B**, **C**, and **D**, since α_∞ enters as a parameter in the definition of $\Gamma_E (\alpha_0)$, cf. Eq. (10), and since this function determines the contact points **B** and **D** on the $-\Gamma_a (\alpha_0)$ line. Points **C** and **A** then indirectly result from this construction and are therefore also functions of α_∞. Experimentally, points **B** and **C** are carried by the same $\Gamma_E (\alpha_0)$ line, at a voltage approximately equal to 160 V, i.e., for about $E = 8 \times 10^4$ V m^{-1}.

2. Difficult return path

We now decrease V backward from the maximum voltage that we previously reached, causing the factor F and the $\Gamma_E (\alpha_0)$ line to decrease proportionally to each other; cf. Sec. IV A 4. The anchoring torque then dominates and drives the c-director towards **S**. Consequently, the operating point **Q** leaves the vicinity of **M** and returns towards **C**, following the same path as on the way from **C** to **M**, but in the reverse direction (red arrow). When point **Q** returns to point **C**, the $\Gamma_E (\alpha_0)$ line is again tangent at **B** to the $-\Gamma_a (\alpha_0)$ line as it was on the forward journey, which means that a further slight decrease in F causes the two lines to intersect at three points, resulting in a three-intersection configuration. However, this event does not produce any change for point **Q**, as the equilibrium between torques Γ_E and $-\Gamma_a$ remains stable at **C**. The c-director and its operating point **Q** therefore cannot jump back towards **B**. In some sense, point **C** works like a *valve* that prevents the direct way back to **B**. Decreasing F again from **C** causes the operating point **Q** to glide, always at quasiequilibrium, along the path towards **D**, that is, along the $-\Gamma_a (\alpha_0)$ line (red arrow again), possibly by means of decreasing voltage steps. Both torques $\Gamma_E (\alpha_0)$ and $-\Gamma_a (\alpha_0)$ remain equal to each other, within the torque uncertainty $\delta\Gamma$, until the $\Gamma_E (\alpha_0)$ and $-\Gamma_a (\alpha_0)$ lines become tangent to each other at point **D**. The configuration is then quite similar to the one encountered when first reaching point **B** in the forward way. So, with the operating point **Q** now at **D**, we decrease voltage and F again towards 0. The two lines separate, which means that **Q** splits into two points, **Q**$'$ and **Q**$''$, that move towards **A** along the green and red lines, respectively. Along this **DA** path, the viscous torque $\Gamma_E(\alpha_0) + \Gamma_a(\alpha_0)$ is negative and drives **Q** back towards **A**. Clearly, points **D** and **A** are analogous to points **B** and **C**, respectively, with the arc **DA** being equivalent to **BC**. Points **Q**$'$ and **Q**$''$ move along both these paths in the same irreversible and out-of-equilibrium manner as on the forward path. Both points **D** and **A** belong to the same line $\Gamma_E (\alpha_0)$ of voltage equal to about 40 V, i.e., for approximately $E = 2 \times 10^4$ V m^{-1}, similarly to the manner points **B** and **C** were previously carried on the same line $\Gamma_E (\alpha_0)$ with an approximate voltage of 160 V. The free flight time along **DA** may thus be estimated using the same method as along the arc **BC**, cf. Sec. IV B 5, with $w_{40} = 2w_{160}$ and $Y_{40} = 2Y_{160}$ now. If such a return journey is really possible, we may anticipate a flight time along **DA** that is about twice as long as on the forward way, i.e., about 10 s.

However, as mentioned in Sec. IV B 6, we observed in some cases on the forward path that the operating point **Q** could not pass through milestone **C**, because too high V-steps would have been necessary, possibly exceeding our maximum voltage of 500 V. On the way back, we need to apply voltages decreasing by steps of the order of $\delta\Gamma$, which indeed are equivalent to *negative* voltage steps. However, according to the estimate of Sec. IV B 6, we have $\delta\Gamma \sim \Gamma$ in the vicinity of **C**, which means that applying a negative $\delta\Gamma$ step may result in an electric torque $\Gamma_E (\alpha_0)$ of about zero. Consequently, both V and F are zero or so. In this case, the operating point **Q** would be directly driven to point **0**, missing the target of point **A**. However, this situation would not be too bad, since a worse configuration could occur if applying a zero voltage

were insufficient to move **Q** towards the arc **0A**. This means that when the anchoring is broken, with **Q** being at **C** or close to **C**, applying a null voltage may not be able to restore **Q** to its original state, close to **0**.

In this case, using relatively large, negative voltage steps as suggested above could result in applying a total negative voltage to the film. Such a negative voltage amounts to changing α_∞ by $\alpha_\infty^{\text{New}} = \pi - \alpha_\infty^{\text{Old}}$, which replaces Fig. 3(c) by Fig. 3(a). The difficulty is then solved. The operating point **Q** quickly connects to arc **0A** somewhere between **0** and the new border milestone **M** at the abscissa $\alpha_\infty^{\text{New}}$. This completely restores the anchoring to its initial state. To come back exactly to the initial configuration, we just need to decrease the voltage to zero, and then to reverse again the voltage sign back to the original sign. The initial α_∞ is thus recovered, and we can restart a new hysteresis loop, identical to the first one.

3. Broken anchoring and hysteresis loop

The three-intersection configuration between the $\Gamma_E\,(\alpha_0)$ and $-\Gamma_a\,(\alpha_0)$ lines provides the opportunity to observe a hysteresis loop when following, as a whole, the paths that the operating point **Q** describes in the torque-anchoring angle diagram of Fig. 3(c). This loop consists of four branches that are alternately reversible (**AB** and **CD**) and irreversible (**BC** and **DA**), or equivalently, at equilibrium and out-of-equilibrium, respectively. Point **Q** follows the reversible **AB** and **CD** paths continuously, being pushed by successive small $\delta\Gamma_E$ steps of an error bar size, when necessary. Conversely, **Q** needs a discontinuity to split into twin operating points **Q′** and **Q″** at a common abscissa α_0, and to freely jump, being driven by a constant applied electric field E, along the irreversible and dissipative dual lines, $\Gamma_E\,(\alpha_0)$ and $-\Gamma_a\,(\alpha_0)$, respectively. This discontinuity has a fortuitous and indeed *indirect origin*, as it is produced by the detachment of both the $-\Gamma_a\,(\alpha_0)$ and $\Gamma_E\,(\alpha_0)$ lines from each other, during their relative motion. The $-\Gamma_a\,(\alpha_0)$ line is fixed, while the $\Gamma_E\,(\alpha_0)$ line moves, primarily controlled by the variations in F or E; cf. Sec. IV A 4. Essentially, their respective shapes do not belong to the same physics. It is worth noting that such a discontinuity in the path that point **Q** follows cannot occur when the $-\Gamma_a\,(\alpha_0)$ and $\Gamma_E\,(\alpha_0)$ lines exhibit only one intersection, since then no discontinuity may arise to break the anchoring.

Though points **C** and **A** are indeed places where the operating point **Q** can land after its flight from **B** and **D**, reciprocally, point **Q** cannot take off back from these points **C** and **A**, because no discontinuity exists there to force **Q** to jump back towards **B** and **D**, as it was on the forward path. This particular property shows that points **C** and **A** indeed work as switches or valves that prevent point **Q** from going back to **B** or to **D**, once running along the reversible paths **CM** or **A0**, respectively; cf. Sec. IV C 2. Consequently, the operating point **Q** cannot describe the **ABCDA** loop in the reverse way.

So, as discussed in Sec. IV B 1, the energy that is dissipated along a path may be estimated from the area that is bounded by the lines $\Gamma_E\,(\alpha_0)$ and $-\Gamma_a\,(\alpha_0)$. When this area is null, the path produces no dissipation and is reversible. Such a property is observed along paths **0AB** and **MCD** exclusively. In the first one, **0AB**, α_0 and E have low values, which means that the anchoring is not broken. In the other path, **MCD**,

the anchoring angle α_0 is close to α_∞. In this second state, the *c*-director on the dislocation is almost aligned along the electric field E, meaning that the anchoring is broken. These two states, nonbroken and broken anchorings, lie on different reversible paths that are connected together by means of dissipative paths **BC** and **DA**. Together with paths **AB** and **CD**, they form a loop. Because of dissipation, the paths are traveled in the **B** to **C** and **D** to **A** directions only, in an irreversible process. As mentioned earlier, these one-way jumps work as valves that build up an oriented loop, i.e., a hysteresis cycle.

However, this hysteresis loop in the torque-anchoring angle diagram cannot be confused with ferromagnetic or ferroelectric hysteresis loops, for several reasons. First, there is an apparent difference in the rotation sense along the torque-anchoring loop, which is observed to be clockwise according to the arrows in Fig. 3(c), instead of being anticlockwise in the ferromagnetic or ferroelectric hysteresis loops. The reason for this is that the diagram should be drawn with *effect-cause axes*, that is, with anchoring angle-torque axes. This leads to exchanging the axes of the diagram, which immediately brings back an anticlockwise rotation. However, there are also real differences. Torque-anchoring angle loops are built here with lines of essentially two distinct types, which are successively reversible and nondissipative, and then irreversible and dissipative. This is different in the ferromagnetic or ferroelectric cases as the nature of the lines continuously changes. Other differences may also be noticed. The hysteresis loop in our case is unique. It joins the **ABCD** milestones for each α_∞ parameter, provided that α_∞ exceeds $130°$. Moreover, when α_∞ is changed, the reversible and nondissipative lines, **AB** and **CD**, remain fixed and never move, while the irreversible and dissipative lines (more precisely, their electric paths, shown as green lines) change according to the values of F and E. Consequently, the milestones that connect them slightly glide along the reversible (red) lines only. Conversely, the hysteresis loops that are observed in ferromagnetism or ferroelectricity are built with one kind of line only. Moreover, when increasing the magnetic or electric field, the different loops appear to be nested inside each other, like "Russian dolls."

4. Additional remarks

An indirect consequence of the breaking of the anchoring, which is marked by a jump in the anchoring angle, is that α_0 cannot continuously cover the entire range of available angles $[0, \pi]$ for any single choice of α_∞. To fill in the gap $[\alpha_B, \alpha_D]$, another α_∞ value should be chosen close to α_D, possibly by changing the voltage sign; cf. Sec. IV A 3. Thus, the anchoring angles α_0 on edge dislocations belong to at least three types of domains: one domain $[0, \alpha_\infty]$ is covered in the one-intersection regime for $\alpha_\infty < 130°$, and two other domains $[0, \alpha_B]$ and $[\alpha_D, \alpha_\infty]$ are obtained in the three-intersection case, i.e., for $130° < \alpha_\infty$. However, these domains may not be sufficient. Other domains $[0, \alpha_\infty]$ should then be used to cover the entire $[0, \pi]$ domain.

It is finally worth noting that the reversibility and irreversibility properties that are discussed here should not be confused with the reversible ability of smectic films to quickly heal up after being submitted to perturbations. Therefore, a short time after less than a complete hysteresis cycle is

completed, the film returns to its initial state. Being a liquid without any defect other than the studied edge dislocation line, the film does not wear out, although it may exhibit irreversible behaviors like solids. However, in our smectic films, which are free of contacts with solids or defects, the irreversibilities are only elusive. Typically, when gradually decreasing E, and thus decreasing α_0 too, while keeping α_∞ constant, we observe that the black interference fringe that had initially disappeared inside the dislocation line, when α_0 was large and close to α_∞, reappears after a significant decrease of α_0. Therefore, provided that a sufficient part of the hysteresis cycle is run, the film completely restores itself to its original state, and is perfectly suitable for another use again.

D. Spring scale

Let us return to the setup and examine the method for measuring the anchoring strength. There are two stages. First, the film functions as a microscale, able to measure small torques produced by a single line of molecules, even though we are more accustomed to dealing with anchoring torques from molecules spread over surfaces. So, we apply an electric torque on the film surface area, limited to w-wide ribbons along each dislocation side; cf. Sec. IV A 2. The resulting distortion produces an elastic torque inside the film that is balanced by the anchoring torque along an edge dislocation line. In this way, the film functions like the spring of a spring scale, providing a direct stress reference based on its own elastic constant $K = N \times 7.5 \times 10^{-21}$ J. More precisely, it allows us to determine the anchoring angle of the *c*-director on the dislocation, α_0, with a noteworthy *amplification factor* of $\sqrt{N}$, Eq. (25). By means of Eq. (10), we can then calculate the anchoring torque $-\Gamma_a(\alpha_0)$ that the dislocation exerts on the film at equilibrium, as a function of α_0. To estimate the error made on the anchoring constant k_a, we may linearize the calculation, which is indeed valid in the small anchoring angle domain of Fig. 2. So, for instance, in the range $\alpha_\infty \sim 1$ rd, the anchoring torque behaves linearly $\sim k_a \alpha_0$. The error that is committed on the anchoring constant k_a is then given by the relation $\delta k_a / k_a = -\alpha_0 / \alpha_0$.

In a next stage, we measure α_0 optically. The film is not only a calibrated spring that weighs the torques applied onto edge dislocations, it also functions as a display for reading the distortion strength. To evaluate the uncertainty we commit when pointing to α_0, we consider the intensity of a fringe obtained from the interference between two light waves perpendicular to a smectic film and that is observed between crossed polarizers, e.g., oriented along the *x* and *y* axes. The total phase shift between these waves is $\varphi = N \varphi_1$, where the phase shift per layer is $\varphi_1 = \frac{2\pi}{\lambda} \Delta n\, l_{\mathrm{Sm}} \sim 6 \times 10^{-3}$ rd. In this expression, λ is the average visible light wave, and $\Delta n\, l_{\mathrm{Sm}} = 0.5 \times 10^{-9}$ m is the path difference per smectic layer. We then rotate both the polarizers by $-\alpha_0$. This rotation shifts the black fringe onto the dislocation, so that in its vicinity, the interference light intensity becomes

$$I \sim \alpha^2\, \varphi^2. \tag{33}$$

More precisely, in the region where $x > 0$, and for $x < w$, Eq. (20) shows that $\alpha(x) \simeq (\alpha_\infty - \alpha_0)\frac{x}{w}$. The $x < 0$ part can then be deduced by symmetry, or simply by replacing x with

$|x|$. Dropping constant terms, the interference intensity reduces at the lowest order to

$$I \sim x^2\, \varphi^2. \tag{34}$$

We reach the uncertainty limits of the fringe location when the light intensity I begins to exceed the minimum observable light intensity. Then, α gives $\delta \alpha_0$. We can thus evaluate the uncertainty that arises from the optical pointing to be $\delta \alpha_0 \sim \frac{1}{N \varphi_1}$. Clearly, increasing the film thickness improves the quality of the optical measurements proportionally, just as increasing the total phase shift improves the interference quality and its reading. In fact, the dominant uncertainty in this experiment seems to originate from the optical detection of the fringe center. It could then be fruitful to use films as thick as possible, but as compensation, their stability could be shortened as well. We could also record the light intensity along the *x*-axis, perpendicular to the dislocation, and fit Eq. (34) on the data. This process could effectively reduce the $\delta \alpha_0$ uncertainty in the α_0 measurements. However, this improved process could again take too much time for measuring thick films before they become destabilized.

Using the amplification factor, $\alpha_0 \sim \sqrt{N}$, on our α_0 measurements, cf. Eq. (25), and dropping the signs, we deduce the relative error we make in measuring the anchoring constant k_a to be

$$\delta k_a / k_a = \delta \alpha_0 / \alpha_0 \sim \frac{1}{N \sqrt{N}}. \tag{35}$$

This estimate shows that the free SmC_A film directly provides an *improvement factor* on the anchoring measurement that is proportional to $N^{3/2} \sim 600$ for $N = 72$ here. It is worth noting that this improvement factor, which is more than two orders of magnitude, is basically due to the mechanical coupling of a one-layer dislocation to an N-layer-thick SmC_A film. Thanks to this improvement factor, the experimental error bar is reduced to $\delta \alpha_0 \sim 5°$, and to $\delta \alpha_0 / \alpha_0 \sim$ 15–20% in relative values; cf. Sec. III. This allows us to deduce an experimental uncertainty $\delta k_a \sim 2.5 \times 10^{-14}$ N on the measured anchoring constant $k_a \sim 1.5 \times 10^{-13}$ N. On the other hand, this result also suggests that for films thinner than $\sim 72 \times 5^{2/3} \sim 25$ layers, the uncertainty should be larger than the measurement itself, making it impossible to perform the measurement.

V. CONCLUSIONS

The anchoring properties of the smectic *c*-director on a 1D edge dislocation, that are analyzed here, extend the widely studied case of the nematic anchoring on 2D solid surfaces. However, we notice several differences that do not only concern the dimension of the anchoring object. In the experiments discussed here, the *c*-director of a 3D SmC_A film connects a 1D edge dislocation line of core size $\sim l_{\mathrm{Sm}} = 3$ nm to a 2D surface that carries an electric polarization *P* on a depth of ~ 1 nm. They are, nevertheless, at a distance from each other equal to the film thickness, since the dislocation is located on the lower SmC_A film surface, while the polarized surface, that receives the electric torque, stands on the upper film surface in contact to the air; cf. Sec. I. The competition that arises between the 1D dislocation line and the 2D polarized surface is thus mediated by a 3D SmC_A film. A 3D distortion then

results in w wide ribbons along both sides of the dislocation. This specific elastic association provides a noteworthy amplification factor of $\sqrt{N}$ in the measurements of the restoring constant k_a, and an overall *improvement factor* of the anchoring measurement of $N^{3/2} \sim 600$, $N = 72$ being the number of smectic layers in the film, cf. Sec. IV D.

Another difference, though less original, is that the anchoring arises between objects made of identical molecules since naturally both the dislocation line and the film bulk only contain MTHAC molecules. Both belong to the same materials, but in different phases that are 1D and 3D liquid-crystal systems, respectively. This specific feature may account for large anchoring angles on dislocations, that extend over exceptionally large spans, up to $[0, \pi]$, in marked contrast with anchoring angles that generally reach a few degrees only, e.g., on 2D solid surfaces. A direct consequence is that the analyses of anchoring data by means of series expansions that basically converge in one point are inappropriate here, even when the convergence point is chosen to be the anchoring angle at rest, i.e., the lowest anchoring energy angle. For this reason, we use Fourier series that have the advantage to converge uniformly over the whole available range of data. The fitting error is then of the same order over the whole angular range. We thus fit second-order Fourier series on our experimental data, i.e., on our measurements of the torque variations as a function of the anchoring angle. However, the quality of our experimental data is insufficient to support fittings of higher-order Fourier series. The main drawback of the Fourier series fits is that they generate artificial oscillations. However, because their amplitudes are lower or in the range of the experimental errors, they indeed have no physical meaning, and we may neglect them.

We tried three limited series expansions in order to make comparisons: a first-order Fourier series, a second-order Fourier series, and a linear expansion based on a one-point convergence at $\alpha_0 = 0$. These data analyses highlight the interest for using series that converge uniformly as Fourier series, in particular, when the torque versus anchoring angle α_0 exhibits weak anchoring conditions as on edge dislocation lines. In turn, this second-order Fourier expansion naturally needs one anchoring constant k_a per order of expansion, i.e., two anchoring coefficients for describing weak anchoring properties that extend over a wide angular domain. They are $k_{a1}^{F2} = 5.07 \times 10^{-14}$N and $k_{a2}^{F2} = 2.42 \times 10^{-14}$N, respectively. For comparison, a first-order approximation may be used in the range of small anchoring angles. The two coefficients then reduce to one anchoring coefficient $k_{a2} = 14.74 \times 10^{-14}$ N, somewhat larger than the direct first-order evaluations, $k_{a0} = 9.37 \times 10^{-14}$ N and $k_{a1} = 11.07 \times 10^{-14}$ N, probably because of a better decoupling from the large angle data in the second-order Fourier analysis.

Another consequence of the exceptionally large range that the anchoring angle α_0 may experience here is the rich state diagram that it may describe. The anchoring state on the dislocation may indeed be represented by an operating point that evolves in a torque-anchoring angle diagram. Two types of processes may occur. The operating point **Q** generally moves along reversible paths, walked in a somewhat "at-equilibrium" fashion, with an infinitely slow velocity of displacement. To accelerate the displacement of **Q**, we apply electric torque

steps of smaller amplitude than the error bar, $\delta\Gamma \sim 0.9 \times 10^{-14}$ N.

When the angle α_∞ of the electric field $\boldsymbol{E}$ relative to the unit vector $\boldsymbol{S}$ (perpendicular to the dislocation, parallel to the film, and oriented from the even- to odd-N film area) is larger than $130°$, the operating point **Q** may follow another type of path with dissipative and out-of-equilibrium properties; cf. Figs. 1 and 3. We can then evaluate the total viscous energy consumed along these out-of-equilibrium paths, as well as the maximum time spent during its free flight section. These paths are one-way paths, as the operating point indeed spontaneously moves from a nonbroken anchoring state with a low anchoring angle α_0 to a broken anchoring state with a high angle α_0, while other one-way paths go in the reverse direction, from a broken anchoring state to a nonbroken one. However, the return way may exhibit a slight difference, as it may require a possible voltage decrease below zero. Overall, the operating point **Q** describes a hysteresis loop that is run in the usual anticlockwise sense if the diagram is drawn with *effect-cause axes*, i.e., with anchoring angles-torques axes, contrary to Figs. 2 and 3. Interestingly, the diagram then exhibits the functioning of a two-state lock, consisting of two valves in series. The two states correspond to low and high levels, with α_0 belonging, on the one hand, to the range $[0, \alpha_0^{max}]$, where α_0^{max} is the anchoring angle at the maximum anchoring torque, and on the other hand, slightly below α_∞, respectively.

Interestingly, the irreversible and dissipative behavior that is observed along paths connecting the two distinct states is not due to interactions with solids or unexpected defects, as the edge dislocation and smectic layers here are perfect 1D and 3D liquid-crystal objects, respectively. The only source of dissipation is fluid viscosity. However, the dissipation in liquids is proportional to v^2 and ω^2, where v and ω are translational and rotational fluid velocities, respectively. Then, reducing velocity may significantly reduce dissipation, too. However, this usual escape from dissipation does not work here, since along dissipative and out-of-equilibrium paths, the operating point indeed flies spontaneously at its own velocity in the torque-anchoring angle diagram. Indeed, as shown in Sec. IV B 3, we can evaluate a maximum time for the free flight along dissipative paths. Such irreversible paths originate from the relative shapes of the lines that show in Fig. 3 the anchoring and electric torques versus angles, $-\Gamma_a (\alpha_0)$ and $\Gamma_E (\alpha_0)$, respectively. They occur when they together exhibit three intersections for $\alpha_\infty > 130°$. Let us notice that this limit of $130°$ between the one and three intersections cases should indeed be specific of the MHTAC molecule, since though the $\Gamma_E (\alpha_0)$ function is general and is valid for all tilted smectics, cf. Sec. II C, the $-\Gamma_a (\alpha_0)$ anchoring torque is not regulated by general laws of physics. The $-\Gamma_a (\alpha_0)$ anchoring torque function is indeed specifically determined by local interactions between MHTAC chemical functions. So, for $\alpha_\infty > 130°$, and for a particular electric field, $\boldsymbol{E}$, the lines that represent the torques, $-\Gamma_a (\alpha_0)$ and $\Gamma_E (\alpha_0)$, may get tangent to each other. Then, a small additional voltage, larger than the error bar, may cause them to separate definitively. Such a mechanism explains the observed discontinuities that initiate the dissipative and irreversible paths, and that lead to an anchoring breaking, or conversely, to its restoration.

So, the liquid nature of the edge dislocation and of the smectic film anchored to it allows them to spontaneously heal back in the very same state as they were before the anchoring breaking, without any erosion effect. Such a perfect restoring does not exist in solid, as their microscopic state unavoidably suffers invisible but real local changes. In practice, however, we need to run about a half hysteresis loop after the anchoring has been broken to completely restore the film exactly in its initial anchoring state.

Let us also notice that basically the mechanism of the c-director anchoring on an edge dislocation may simply be understood from a local and partial melting of the dislocation edge that continuously increases with the c-director anchoring angle. More specifically, we suggest that SmC_A prominent molecules in the dislocation edge enter as a thorn in the nematic environment, all the more deeply as the c-director anchoring angle increases on the dislocation These molecules consequently partially melt upon contact with the nematic phase. This melting process requires an additional energy which indeed identifies with the anchoring energy that the applied torque transmits to the dislocation.

These experimental results may provide an approach to the interactions that exist between parallel edge dislocations. They could help to understand their attraction and sticking properties to one another for building multiple edge dislocations. From the anchoring properties of the c-director on edge dislocations that are discussed and analyzed above, we may now calibrate the amplitude of the thermodynamic c-fluctuations that take place between two simple edge dislocations. This should give access to the pseudo-Casimir force that the dislocations exert on each other, a force that is equivalent to the Casimir force, the c-director fluctuations replacing the Casimir electromagnetic fluctuations. This new force could explain the relative stability of multiple dislocations when submitted to an electric field of limited strength. The multiple edge dislocations could then be understood as being made of simple edge dislocations interacting at some distance apart from each other by means of pseudo-Casimir interactions. Such an interaction could be efficient at intermediate and definite distances depending on the strength and direction of an applied electric field [12]. Because of the antagonistic anchoring conditions between two identical edge dislocations, parallel and close to each other, we anticipate that their individual anchoring angles α_0 could significantly exceed $90°$, so that the knowledge of the c-director anchoring properties over a wide angular range could indeed be essential.

[1] Y. Galerne and L. Liebert, Smectic-O Films, Phys. Rev. Lett. **64**, 906 (1990).

[2] Y. Galerne, Optical analysis of the surface smectic-O film, Europhys. Lett. **18**, 511 (1992).

[3] Y. Galerne and L. Liebert, Antiferroelectric Chiral Smectic-O* Liquid Crystal, Phys. Rev. Lett. **66**, 2891 (1991).

[4] E. Gorecka, A. D. L. Chandani, Ouchi Y, H. Takezoe, and A. Fukuda, Molecular orientational structures in ferroelectric, ferrielectric and antiferroelectric smectic liquid crystal phases as studied by conoscope observation, Jpn. J. Appl. Phys. **29**, 131 (1990).

[5] G. Heppke, P. Kleineberg, D. Lotzsch, S. Mery, and R. Shashidhar, Do the smectic O and the antiferroelectric smectic C phases belong to the same phase type? Mol. Cryst. Liq. Cryst. **231**, 257 (1993).

[6] V. Candel and Y. Galerne, Anchoring Strength Onto Simple Surface Edge Dislocations in an Induced Smectic-O Film, Phys. Rev. Lett. **70**, 4083 (1993).

[7] A. Scharkowski, G. P. Crawford, S. Zumer, and J. W. Doane, A method for the determination of the elastic constant ratio K33/K11 in nematic liquid crystals, J. Appl. Phys. **73**, 7280 (1993).

[8] J. F. Strömer, E. P. Raynes, and C. V. Brown, Study of elastic constant ratios in nematic liquid crystals, Appl. Phys. Lett. **88**, 051915 (2006).

[9] M. A. Osipov and S. Hess, Elastic constants of nematics: Comparison between molecular theory and computer simulations, Liq. Cryst. **16**, 845 (1994).

[10] D. Venkata Sai, G. Mirri, P. H. J. Kouwer, R. Sahoo, I. Musevic, and S. Dhara, Unusual temperature dependence of elastic constants of an ambient-temperature discotic nematic liquid crystal, Soft Matter **12**, 2960 (2016).

[11] V. Candel and Y. Galerne, Anomalous anisotropy of the elastic constants in the induced smectic O film, Liq. Cryst. **15**, 541 (1993).

[12] P. Ziherl, F. K. P. Haddadan, R. Podgornik, and S. Zumer, Pseudo-Casimir effect in nematic liquid crystals in frustrating geometries, Phys. Rev. E **61**, 5361 (2000).

[13] A. Rapini and M. Papoular, Distorsion d'une lamelle nématique sous champ magnétique conditions d'ancrage aux parois, J. Phys. (Paris) **30**, C4-54 (1969).

[14] K. H. Yang and C. Rosenblatt, Determination of the anisotropic potential at the nematic liquid crystal-to-wall interface, Appl. Phys. Lett. **43**, 62 (1983).

[15] G. Barbero, N. V. Madhusudana, J. F. Palierne, and G. Durand, Optical determination of large distortion surface anchoring torques in a nematic liquid crystal, Phys. Lett. A **103**, 385 (1984).

[16] See, e.g., https://en.wikipedia.org/wiki/Convergence_of_Fourier_series.

[17] H. Yokoyama and H. A. van Sprang, A novel method for determining the anchoring energy function at a nematic liquid crystal–wall interface from director distortions at high fields, J. Appl. Phys. **57**, 4520 (1985).

[18] A. J. Herbert, Transition temperatures and transition energies of the p-n- alkoxy benzoic acids, from n-Propyl to n-Octadecyl, Trans. Faraday Soc. **63**, 555 (1967).

[19] D. Subacius, V. M. Pergamenshchik, and O. D. Lavrentovich, Measurement of polar anchoring coefficient for nematic cell with high pretilt angle, Appl. Phys. Lett. **67**, 214 (1995).

[20] M. Vilfan and M. Copic, Azimuthal and zenithal anchoring of nematic liquid crystals, Phys. Rev. E **68**, 031704 (2003).

[21] Y. Galerne, J. L. Martinand, G. Durand, and M. Veyssié, Quasielastic Rayleigh Scattering in a Smectic C Liquid Crystal, Phys. Rev. Lett. **29**, 562 (1972).

[22] S. Meiboom and R. C. Hewitt, Rotational Viscosity of a Smectic-C Liquid-Crystalline, Phys. Rev. Lett. **34**, 1146 (1975).

[23] A. Levstik, Z. Kutnjak, C. Filipic, I. Levstik, Z. Bregar, B. Zeks, and T. Carlsson, Dielectric method for determining the rotational viscosity in thick samples of ferroelectric chiral smectic-C' liquid crystals, Phys. Rev. A **42**, 2204 (1990).

[24] S. Krishna Prasad, S. M. Khened, V. N. Raja, and B. Shivkumar, Measurement of rotational viscosity in the Smectic C* phase, Ferroelectrics **121**, 319 (1991).